Title

Enhanced Robot-Environment Interfaces to Improve Locomotion on Natural Terrain

Author

Lathrop, Emily

Publication Date

2022

Peer reviewed|Thesis/dissertation

UNIVERSITY OF CALIFORNIA SAN DIEGO

Enhanced Robot-Environment Interfaces to Improve Locomotion on Natural Terrain

A dissertation submitted in partial satisfaction of the
requirements for the degree
Doctor of Philosophy

in

Engineering Sciences (Mechanical Engineering)

by

Emily Lathrop

Committee in charge:

Professor Nick Gravish, Co-Chair
Professor Michael T. Tolley, Co-Chair
Professor Henrik Christensen
Professor Tania Morimoto

2022

The dissertation of Emily Lathrop is approved, and it is acceptable in quality and form for publication on microfilm and electronically.

University of California San Diego

2022

TABLE OF CONTENTS

Dissertation Approval Page iii

Table of Contents iv

List of Figures vi

Acknowledgements vii

Vita ix

Abstract of the Dissertation x

Chapter 1 Introduction 1
1.1 Shear Strengthened Granular Jamming Feet for Improved Performance over Natural Terrain: 3
1.2 Embodied Intelligence in Leg Design Enables Crevasse Traversal in Small Ground-based Robots: 4
1.3 Local Fluidization of Granular Media for Directional Force Reduction in Digging Robots: 5

Chapter 2 Shear Strengthened Granular Jamming Feet for Improved Performance over Natural Terrain 6
2.1 Introduction 6
2.2 Design and Fabrication 9
2.3 Characterization 10
2.3.1 Ability to Resist Shear Forces 10
2.3.2 Ability to Conform Around Obstacles 11
2.4 Validation on Hexapod 12
2.4.1 Speed Benefit 14
2.4.2 Duty Cycle Necessary to Reach Desired Foot Trajectory . . 16
2.4.3 Maximum Net Thrust 17
2.5 Conclusion 18

Chapter 3 Embodied Intelligence in Leg Design Enables Crevasse Traversal in Small Ground-based Robots 21
3.1 Introduction 21
3.2 Background 24
3.2.1 Robots in Confined Spaces 25
3.3 Design 27
3.3.1 Leg Geometry 27
3.3.2 Leg Fabrication 28
3.3.3 Robot Platform 29

3.4 Modeling and Simulation . . . 29
3.4.1 Leg Model . . . 29
3.4.2 Walking Robot Simulation . . . 31
3.5 Results . . . 32
3.5.1 Model Fitting . . . 32
3.5.2 Optimal Leg Shape . . . 32
3.5.3 Optimal Leg Stiffness . . . 34
3.5.4 Leg Stiffness Validation on Robot Platform . . . 36
3.5.5 Speed Dependence on Leg Length . . . 36
3.5.6 Robot Demonstrations . . . 38
3.6 Conclusion . . . 41

Chapter 4 Local Fluidization of Granular Media for Directional Force Reduction in Digging Robots . . . 43
4.1 Introduction . . . 43
4.2 Background: Fluidization in Granular Media . . . 44
4.3 Physics of Fluidization . . . 45
4.3.1 Experimental Setup . . . 46
4.3.2 Effect of Input Pressure . . . 46
4.3.3 Effect of Surface Area . . . 48
4.3.4 Effect of Sheet Thickness . . . 48
4.4 Fluidizing Probe Attached to Robot Arm . . . 48
4.4.1 Vertical Force Reduction . . . 51
4.4.2 Horizontal Force Reduction . . . 51
4.5 3D RFT with Fluidization Scaling Factor . . . 53
4.6 Robot Demonstration . . . 55
4.6.1 Robot Performance . . . 55
4.7 Discussion . . . 59

Chapter 5 Summary . . . 60

Bibliography . . . 64

LIST OF FIGURES

Figure 2.1: Hexapod with granular jamming feet 8
Figure 2.2: Shear force tests 10
Figure 2.3: Area of contact tests 13
Figure 2.4: Foot designs and terrains tested 13
Figure 2.5: Gait Sequence 14
Figure 2.6: Speed over varying ground 15
Figure 2.7: Motor duty cycle to reach desired foot trajectories 16
Figure 2.8: Drawbar pull test for maximum thrust 18

Figure 3.1: Robot with passively telescoping legs 22
Figure 3.2: Current landscape of legged robot locomotion in confined spaces 26
Figure 3.3: Leg design and model 30
Figure 3.4: Force vs. displacement test on a single leg 33
Figure 3.5: Maximum achievable passive leg compression 35
Figure 3.6: Simulation to determine optimal spring stiffness 37
Figure 3.7: Robot walking speed in narrow channels 39
Figure 3.8: Robot demonstrations 40

Figure 4.1: Vertical intrusion experiments on a diffusive sheet 47
Figure 4.2: Effect of surface area and sheet thickness on force 49
Figure 4.3: Fluidizing probe with independently fluidized surfaces attached to a robot arm 50
Figure 4.4: Vertical force reduction over complex paths 52
Figure 4.5: Horizontal force reduction over complex paths 54
Figure 4.6: 3D RFT with a pressure-depth dependent scaling factor 56
Figure 4.7: Anchoring robot using granular fluidization for locomotion 57
Figure 4.8: Actuation for subterranean locomotion 58

ACKNOWLEDGEMENTS

I would like to thank my advisors Professor Michael Tolley and Professor Nick Gravish for the opportunity to complete a PhD, and for the research training, manuscript feedback, and other guidance that I have received during my time here. I would also like to thank my committee members Professor Henrik Christensen and Professor Tania Morimoto for their support and feedback.

I am grateful to my lab-members both in the Bioinspired Robotics and Design Lab and the Gravish Lab, both past and present. Thank you for the insightful research discussions and the companionship during both early mornings and late nights. I have enjoyed not only the research conversations but also the meandering ones, and I have enjoyed the opportunity to learn and participate in such a wide variety of research niches.

I would like to thank my family and friends for their support during my time at UCSD, especially the triathlon team for making sure that I always make time to stay active, and for always indulging in my coffee ride requests.

The following acknowledgements are to satisfy the requirements of the University of California San Diego.

I acknowledge the financial support of the National Science Foundation Graduate Research Fellowship Program under Grant No. DGE-1650112.

Chapter 2, in full, is a reprint of the material "Shear Strengthened Granular Jamming Feet for Improved Performance over Natural Terrain" as it appears in the 3rd IEEE International Conference on Soft Robotics (RoboSoft 2020). Lathrop, Emily; Adibnazari, Iman; Gravish, Nick; Tolley, Michael T., RoboSoft 2020. The dissertation author was the primary investigator and author of this paper.

Chapter 3, in full, has been submitted for publication as "Embodied Intelligence in Leg Design Enables Crevasse Traversal in Small Ground-based Robots" as it may appear in Advanced Intelligent Systems. Lathrop, Emily; Tolley, Michael T.; Gravish, Nick. The dissertation author

was the primary investigator and author of this paper.

Chapter 4, or portion thereof, is being prepared for publication of the material. Lathrop, Emily; Jadhav, Saurabh; Tolley, Michael T.; Gravish, Nick. The dissertation author was the primary investigator and author of this paper.

VITA

2014	Bachelor of Science in Computer Engineering, University of Maryland College Park
2020	Master of Science in Engineering Sciences (Mechanical Engineering), University of California San Diego
2022	Doctor of Philosophy in Engineering Sciences (Mechanical Engineering), University of California San Diego

PUBLICATIONS

Lathrop, E., Jadhav, S., Gravish, N., Tolley, M. T., Local Fluidization of Granular Media for Directional Force Reduction in Digging Robots,*In Prep.*.

Lathrop, E., Gravish, N., Tolley, M. T., Embodied Intelligence in Leg Design Enables Crevasse Traversal in Small Ground-based Robots, Advanced Intelligent Systems, *In Review*.

Lathrop, E., Adibnazari, I., Gravish, N., Tolley, M. T., Shear strengthened granular jamming feet for improved performance over natural terrain, *IEEE International Conference on Soft Robotics (RoboSoft)*, May 2020, pp. 388-393.

Shih, B., Lathrop, E., Adibnazari, I., Martin, R., Park, Y. L., Tolley, M. T., Classification of components of affective touch using rapidly-manufacturable soft sensor skins. *IEEE International Conference on Soft Robotics (RoboSoft)*, May 2020, pp. 182-187.

ABSTRACT OF THE DISSERTATION

Enhanced Robot-Environment Interfaces to Improve Locomotion on Natural Terrain

by

Emily Lathrop

Doctor of Philosophy in Engineering Sciences (Mechanical Engineering)

University of California San Diego, 2022

Professor Nick Gravish, Co-Chair
Professor Michael T. Tolley, Co-Chair

Mobile robots can be used in unstructured environments that are dangerous or difficult for humans to access. As mobile robots become increasingly prevalent in society, they are beginning to be deployed to more natural environment spaces. Natural environments feature diverse sets of challenges that are terrain specific, for example robot strategies and morphologies needed for movement over sand dunes differs greatly from those needed for movement through dense forest underbrush, or through caves systems. As we seek to extend the range of robots from the human engineered spaces that they mostly inhabit today, new robot designs and movement strategies are needed in order to ensure robust and efficient locomotion. To date, much work has been done on

complex sensing and control strategies to compensate for irregular environmental features, but these control strategies often involve expensive components and are computationally expensive. Alternatively, we can use morphology solutions to offload computation to the body of the robot, reducing sensor needs and freeing computational power to be used for other tasks. To achieve this, we can harness new actuation strategies, unconventional materials, and novel robot appendage designs to modulate robot-environment interactions and improve performance. This dissertation describes the design of robot-environment interfaces that improve physical interactions between a robot and it's environment to enable locomotion through that environment. First, I create shear-strengthened variable stiffness robot appendages that can create reliable ground contact even over irregular terrain. I demonstrate designs for reducing shear failure and increasing robot speed and traction. Next, I present a robot featuring directionally compliant telescoping appendages that allow it to passively compress to enter both vertically and horizontally confined spaces without sacrificing performance over open terrain features such as steps and rock gardens. Finally, I present a method for improving the digging capabilities of mobile robots through directional drag reduction with porous sheets and granular fluidization. Overall, these results demonstrate methods for designing robot morphologies to elicit beneficial interactions when moving through target environments.

Chapter 1

Introduction

There has been recent interest in expanding the range of spaces that robots inhabit from human-engineered spaces into natural terrain environments. When deployed in natural environments, robots can be used for applications ranging from exploration to search-and-rescue. Robots are ideal for use in environments that are either dangerous or inaccessible to humans such as deep caves, extraterrestrial surfaces, and disaster zones. However, designing robots that can move successfully in natural environments is a challenging task. Success depends on being able to navigate through obstacles of a large range of sizes, and move within terrain which can be composed of many diverse properties. Examples of challenging terrain include loose rocks and sandy surfaces, where non-cohesive ground can shift and flow depending on loading conditions. Failure cases often include loss of traction or obstacles that can't be overcome due to robot geometry. To design robots that are robust to these scenarios, we focus on the interface between a robot and it's environment, and how we can modify the ways that a robot interacts with it's surroundings to elicit favorable interactions with terrain to increase the robot's capabilities.

In natural terrain, legged robots often have an advantage over their wheeled counterparts because they can adjust their posture for stability and choose their footholds with precision.

Classes of robots that have demonstrated successful locomotion over natural terrain include quadruped robots [1, 2, 3, 4], hexapod robots [5, 6, 7, 8, 9], snake-like robots [10, 11, 12, 13], and wheel-leg transformer robots [14, 15, 16, 17]. Often, the ability to traverse natural terrain depends on complex planning and stabilization behaviors [4] to choose footholds that result in favorable foot-ground interactions.

Alternatively, some robots use embodied intelligence to compensate for variations in terrain. This can include strategies such as dynamically stable gaits [5] or the use of compliant appendages [18]. Embodied intelligence refers to how actor/robot behavior is influenced by the physical interactions between the actor and it's environment [19]. By intelligently designing robot bodies to interact in certain ways with it's environment, control loops can be built into these physical interactions that reduce the need for feedback control [20, 21]. This is also known as morphological computation [20]. In Chapter 3, I design a robot that can use it's morphology to passively modify it's leg length through interactions with narrowing channels.

The field of soft robotics offers an exciting avenue for the design of robots with embodied intelligence [22]. Soft robotics refers to the design of robotic systems using soft, elastic, and flexible materials. This can be contrasted to traditional approaches, which typically use rigid materials such as aluminum, steel, and plastic [23]. Novel soft materials and actuators can enable robots to compensate for unexpected contact in complex environments through deformation and compliance [23]. One such example is seen in the use of soft gecko adhesives for climbing robots [24, 25]. Another example can be seen in the use of compliant robot feet that can increase stability over rough ground [26, 27]. Soft actuators such as granular jamming grippers [28] can allow robots to modify their stiffness to conform to objects. This is done using vacuum to control the amount of air within a granular material, which controls the compaction and flow of particles, altering stiffness. In Chapter 2, I demonstrate how we can use granular jamming to design compliant robot feet that can conform to rough terrain and increase robot traction.

When granular materials instead compose the environment that a robot is moving through

(examples include subterranean locomotion in sand and dirt), we can again use the properties of the granular materials to design robots that can move through them. Granular fluidization involves passing a fluid such as air or water through a granular material, disturbing force chains found when the material is static, and allowing the grains to flow with fluid-like properties [29]. In Chapter 4, I examine how we can use fluidization in order to directionally alter drag forces and enable a digging robot.

In this dissertation, I design robot systems and morphologies to improve locomotion in three environments: 1) small rough ground such as rocks and wood chips; 2) large obstacles that appear as tunnels and high walls, and 3) subterranean locomotion in granular media. In each of these environments, I study the benefits of modifying contact surfaces between a robot and it's environment in order to improve physical interactions such as increasing traction, or reducing drag. In the first chapter, I improve robot traction on on loose terrain using shear-strengthened granular jamming appendages. In the second chapter, I use passively-collapsible appendages to enable robot locomotion in confined spaces. In the third chapter, I examine how we can use the properties of fluidized granular media to enable subterranean locomotion. Below I describe the main contributions and key results from each chapter:

1.1 Shear Strengthened Granular Jamming Feet for Improved Performance over Natural Terrain:

Walking on natural terrain like soil and rock is a challenging problem that has been approached from a variety of strategies such as using sophisticated control methods, compliant legs, and compliant feet. In Chapter 2, we explore how to modify granular jamming feet for walking applications by adding stabilizing internal structures. Previous work has explored how granular jamming technology can be used to create compliant and stiffness changing feet that enable locomotion over a diverse range of natural terrain by allowing robot feet to conform

around 3D multicomponent terrain such as wood chips and gravel and stiffen, preventing slip. We show that adding internal structures to granular jamming membranes can increase the force they are able to resist without slipping by 1.5× while maintaining their ability to conform around obstacles. When attached to a robot, we see increases in speed of up to 1.4×, decreases in the duty cycle necessary to reach desired foot trajectories of up to 5%, and increases in traction force of up to 1.2x over a diverse set of natural terrain.

1.2 Embodied Intelligence in Leg Design Enables Crevasse Traversal in Small Ground-based Robots:

Small ground-based robots show promise for locomotion on complex surfaces. However, the terrain that centimeter-scale robots experience presents substantially more height variation and constriction (both relative to body size) than what is experienced by larger meter-scale walking robots. To contend with this terrain complexity, robots typically require high degree-of-freedom (DOF) limbs. However, for small robot platforms, this approach of high DOF legs are impractical due to actuator limitations. This presents an opportunity to design robots with embodied intelligence to achieve versatile movement in confined spaces and increase the range of spaces that robots can access in unknown environments. In Chapter 3, a novel robot appendage is developed that can passively compress in a programmed direction in response to environmental constrictions. A robot equipped with these appendages can enter narrow spaces down to 72% of the robot's sprawled body width as well as low ceilings down to 68% its free standing height. The robot is able to step onto and over small terrain features (1.6× hip height) and navigate various natural terrain types with ease. Our results show that these compressible appendages enable versatile robot locomotion for robot exploration in previously unmapped environments.

1.3 Local Fluidization of Granular Media for Directional Force Reduction in Digging Robots:

Although nature offers many examples of animals that dig and burrow, so far subterranean locomotion has been a challenging task for robots due to the high forces involved. Granular fluidization, a method used by clams, squids, and wrasse fish to enable fast subterranean burrowing, offers a method for reducing these high forces by modifying the properties of the surrounding granular material. In Chapter 4, we characterize the physics of the fluidization generated by diffusive panels and determine a scaling factor that can be used in conjunction with resistive force theory to predict forces on fluidizing plates in granular media. Next, we demonstrate that we can directionally alter drag forces on a moving body through the use of fluidizing panels built into the walls of the body. We then show that this strategy can be used to enable locomotion in a simple anchoring-extension robot.

Chapter 2

Shear Strengthened Granular Jamming Feet for Improved Performance over Natural Terrain

2.1 Introduction

The two main design approaches for mobility over natural terrain are wheels and legs. Historically, wheeled robots have been used for applications such as exploring the surface of mars or navigation through disaster zones, but often wheeled vehicles perform poorly when confronted with features such as obstacles, gaps, or soft and deformable terrain such as sand or mud [30]. In contrast, legged robots have more success at stepping on or over obstacles [30], but often fail when they are unable to create a stable foothold. Failure includes characteristics such as sinking into terrain instead of making forward progress and slipping when attempting to push off during a stride. It is advantageous to have robots that are able to walk effectively over natural terrain, since these are the situations where we would most like robots to take the place of humans due to

safety (eg. disaster and conflict zones) or accessibility concerns (eg. extraterrestrial exploration).

Robot feet are usually made from stiff material and are not capable of varying shape or stiffness while walking. However, when transitioning between terrain types it would be advantageous to have robot feet that can actively change shape or stiffness to optimize ground contact forces and traction. For example, on sand it may be advantageous to have a flat foot with a large surface area to prevent sinking, but over a pockmarked lunar surface it may be advantageous for part of the foot to sink into a crevice and grip onto it.

Granular jamming appendages offer a solution in which secure, rigid footholds can be made yet feet can be soft when first stepping down to adapt and conform to the surface profile. Granular jamming technology can enable re-configurable feet – we hypothesize that they can allow a foot to spread out and conform around obstacles as it touches down, and then stiffen, providing a platform to push off from. But adapting granular jamming for use in feet has its own obstacles, such as an inability to withstand large shear forces without failing [31], especially at the interface of the granular matter and the collar at the base of the foot (Fig. 2.4b).

Previous work has shown that adding reinforcing structures can increase the peak shear force that a dry granular media is able to withstand [32]. In this paper we aim to adapt granular jamming for use as a robot foot by adding internal structures to allow the feet to better resist shear forces. We then attach these feet to a commercially available hexapod and characterize it's performance over natural terrain.

The jamming of granular particles has been used to explain how mechanical stability arises from disordered particulate systems as the packing fraction increases [33, 34]. Researchers have used this stiffness changing property of granular materials to design variable stiffness actuators by enclosing particles in a membrane at a packing fraction near the jamming transition. The particle filled membrane is soft and can conform around obstacles in its normal state but when the packing fraction is increased slightly via vacuum, the particles jam, and the actuator becomes rigid. Granular jamming actuators have been used for a variety of robotic applications including

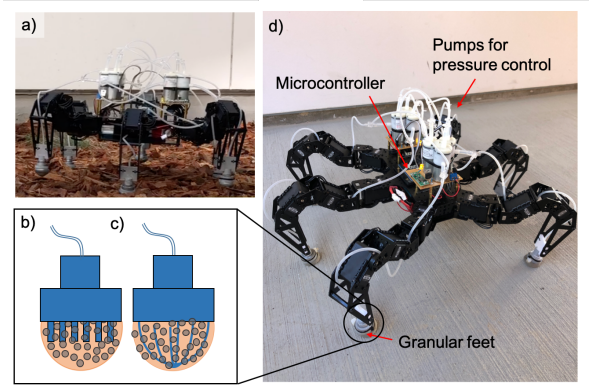

Figure 2.1: Hexapod with granular jamming feet. a) Untethered hexapod with attached feet and on-board fluidic control on wood chips. b) Foot design composed of elastic membrane filled with granular media and reinforced with rigid rods. c) Foot design composed of elastic membrane filled with granular media and reinforced with abrasive fibers. d) Schematic of hexapod.

grippers with simple control and actuation systems [35, 36], jamming skin enabled locomotion [37], variable stiffness haptic devices [38, **?**], and stiffness changing manipulators for minimally invasive surgery [39].

To date, several robot designs with simple actuation strategies have been explored for navigating unstructured terrain including rigid, c-shaped legs [40], kirigami skins [41], jamming skin enabled locomotion [37], and 3D printed soft actuators [18], but all these designs still do not feature feet that are able to conform around obstacles. Researchers have also explored using simple rigid feet with sophisticated control strategies [42, 43] to enable effective locomotion. While this has allowed robots to walk over a wider range of terrain, walking speed is very slow as each step is computationally expensive.

Previous work has begun exploring how granular jamming actuators can be used as robot feet [44, 31], but so far researchers have only demonstrated locomotion on flat surfaces and single, small obstacles placed on flat surfaces, not on natural or irregularly shaped terrain. We aim to address some of the challenges of using granular jamming actuators as robot feet and expand upon the range of surfaces that these feet are able to walk over. One of the main challenges for in doing this is that a foot has to support shear as well as normal forces, whereas in a task such as

gripping, previous work has often explored only normal pull-off forces [35]. In granular jamming, unstable, fragile jammed states are common in shear [45], which puts granular jamming actuators at a disadvantage for use in walking.

We propose to address this challenge by adding internal structures inside the granular jamming casing to increase the force the foot can withstand in shear. The inspiration for the design of these structures is drawn from natural and engineered slope stabilization techniques to reduce landslides and lessen erosion. These methods include using plant roots to naturally stabilize a slope [46] or adding rigid support elements such as piles [47]. We then attach this modified granular jamming foot to a robot and quantify the performance benefits of both passive and active jamming over various types of natural terrain.

2.2 Design and Fabrication

Our foot consisted of a reversible granular jamming sack composed of a nonporous elastic membrane (latex) filled with a granular media (coffee grounds). The elastic membrane was attached at its widest point to a stiff ankle printed from PLA (Fig. 2.1 b, c), resulting in a foot in the shape of a half sphere (diameter 2.6 cm). In its normal state the sack was deformable but negative pressure was applied, the particles jammed together and turned solid. Positive pressure was then used to reset the sack to its unjammed state. For the characterization tests, we controlled the internal pressure of the sack using a fluidic control board [48] capable of generating 10 psi of negative pressure.

We then added one of two classes of internal structures that protruded into the membrane from the base (Fig. 2.1 b, c). The structures were inspired by structural engineering techniques such as pilings and fiber-reinforced soil or concrete, commonly used for increasing structural integrity and resisting shear loads. The first class of internal structures consisted of 3D printed PLA rods of radius 1 mm or 2 mm and length 6 mm in both cases. The base and rods were printed

as one piece out of PLA. For the 1mm radius rods, the spacing of the rods consisted of two rings of 12 rods each, spaced 7 mm and 10 mm from the center. For the 2 mm radius rods, the spacing consisted of one ring of 12 rods, spaced 7.5 mm from the center. The second class consisted of abrasive fiber cords of diameter .46 mm, .76 mm and 1.4 mm coated with aluminum oxide grit (Mitchell Abrasives). The cords were mounted into blind holes printed into the PLA base, and sit entirely within the granular media, not contacting the latex membrane. We then characterized the performance of these structures.

2.3 Characterization

2.3.1 Ability to Resist Shear Forces

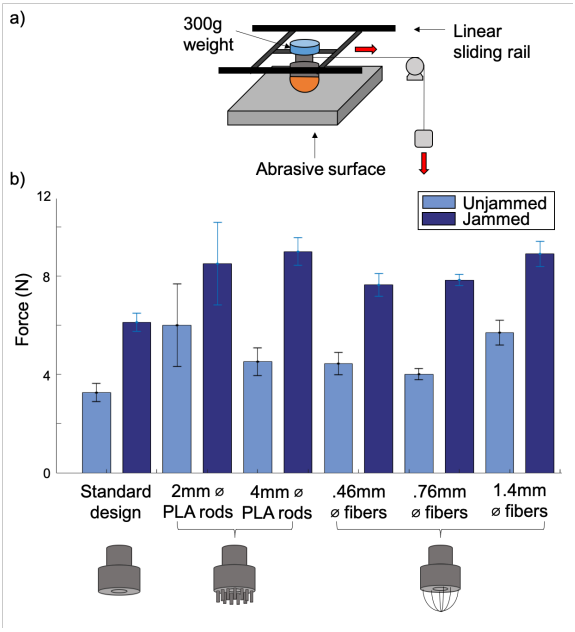

Figure 2.2: Shear force tests. a) Shear setup. b) Passively and actively jammed shear strength before slipping on a pebbled surface.

We characterized the shear force that each foot is able to resist without slipping in both the passively jammed (no vacuum but jammed due to the vertical weight) and actively jammed

cases. To do this, the foot is placed in contact with a representative natural surface composed of rough pebbles secured to a surface (average diameter = 0.5 cm) and vertically loaded with a 300g weight (roughly 1/6 of our hexapod weight). The foot is attached to a rail that constrains it to travel horizontally while allowing it to move freely vertically (Fig. 2.2a). We use a pulley system to apply increasing tangential force and measure the force at which the foot begins to slip.

In the passively jammed case (Fig. 2.2b), all designs with internal structures increased the shear strength before slipping compared to the standard design, with the small diameter stiff rods and the large diameter abrasive fibers performing the best. For these two cases, the diameter of the internal structures were similar (1 mm and 1.4 mm for the rods and fibers respectively).

When jammed, both the internal PLA rods and the abrasive fibers increased the shear strength before slipping, compared to the standard design (Fig. 2.2b). As the diameter of the internal structures increased, the shear strength increased (for each type of internal structure).

2.3.2 Ability to Conform Around Obstacles

Although adding internal structures can increase the strength of our feet, the structures also have the potential to decrease the foot's ability to conform around obstacles in its unjammed state compared to a foot without internal structures. This is due to the fact that the internal structures do not experience a stiffness change when transitioning from jammed to unjammed, and maintain their original stiffness throughout a cycle. This results in an increased composite stiffness of the foot while unjammed due to the contribution of the stiff internal structures.

We used Frustrated Total Internal Reflection (FTIR) to measure the area of contact between two surfaces - the granular foot and the ground adjacent to an obstacle the foot was placed partially over. We built an FTIR sensor composed of white LEDs illuminating the edge of a rectangular polycarbonate plate. We then built a platform over the sensor that allows the foot to be displaced vertically around an obstacle on the plate (Fig. 2.3a). Images were captured with minimal ambient light and a reference frame was used to subtract out ambient light in post

processing. By measuring contact area, we aim to measure which internal structures do not decrease the ability of the foot to conform around obstacles.

A 500g weight was applied at the ankle of the foot for a constant normal loading of the foot onto the plate and step. When the foot made contact with the plate, it illuminated the contact area. Using a camera, we measured the contact area that a passive soft foot could achieve around an obstacle - a rigid acrylic step half the height of the foot. All tests were done in the passively jammed state with 5 trials for each design.

As seen in Fig. 2.3b, the rigid PLA rods limit the ability of the foot to conform around a step to about 50% of the performance of a foot with no internal structures. The thin fiber design was able to achieve a similar contact area to the standard design, the mid-thickness fibers performed about 2.5$\times$ as well as base design, and the thickest diameter of fibers performed about 75% as well as the standard design. We hypothesize that the thickest fibers may behave similarly to the rigid PLA rods in that they limit the softness of the foot. We hypothesize that the mid-thickness fibers performed well due to the fact that the fibers are flexible enough to conform around obstacles but also stiff enough to push against the membrane to reset the foot back to its original shape between trials, resetting the compaction of the granular media inside the foot.

As a result of the previous two tests, we decided to implement the mid thickness abrasive fiber design onto a robot since it performed well in shear as well as increased the ability of the foot to create ground contact around obstacles.

2.4 Validation on Hexapod

We then validated this new foot design on a commercially available hexapod (Arcbotix, Fig. 2.1d). We attach either 1) the stock feet composed of a 5mm thick laser cut acrylic plate (width $\approx$1 cm) with a rubber pad encasing the acrylic of thickness 1.5 mm, 2) the base granular design without any reinforcing structures, or 3) a fiber reinforced granular jamming foot (Fig.

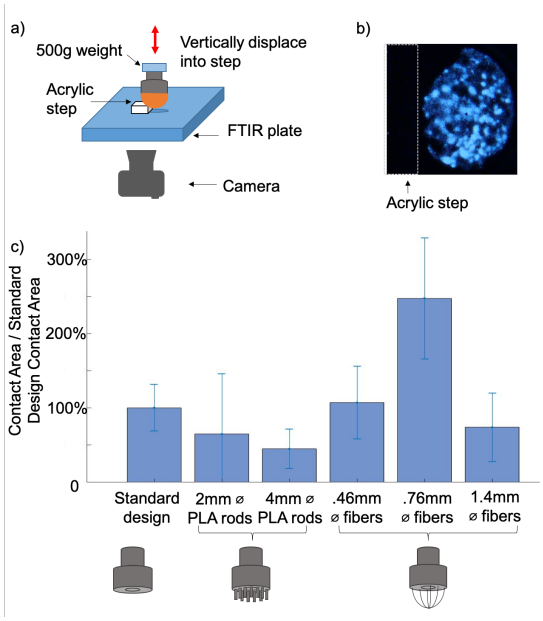

Figure 2.3: Area of contact tests. a) Total internal reflection setup for area of contact tests. b) Sample camera image of FTIR plate illuminating contact area of the foot with the acrylic step outlined with a white dashed line. c) Results for area of contact tests, y axis is total contact normalized against contact area for standard design.

2.4a,b,c respectively). We designed and fabricated an on-board pneumatic system similar in function to the fluidic control board presented in [48]. The system is capable of generating negative pressure (-10 PSI) to control the jamming of the feet, and positive pressure (1 PSI) to unjam the foot between each step by adding connections to the intake and outlet of a pump, respectively.

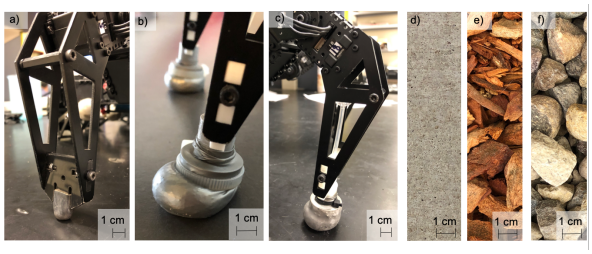

Figure 2.4: Foot designs and terrains tested. a) Rigid foot. b) Granular jamming foot, base design, displaying failure in shear. c) Granular jamming foot with fiber reinforcement. d) Concrete (flat ground). e) Wood chips. f) Loose Rock.

For the active foot tests, we jammed the foot in sequence with the gait (Fig. 2.5). We chose

an alternating tripod gait since it is a common, stable gait used by many hexapods. Each foot is jammed immediately after it comes in contact with the ground and the foot has time to conform around its environment (t = 0 s in the gait cycle). The jamming action takes approximately 0.5 s to rigidify. Once the stance phase is completed the foot is then unjammed with positive pressure and the foot lifts. The time it takes the foot to fully jam once negative pressure is applied ($\approx$ 0.5 s) is negligible compared to the time for one step cycle (3 s).

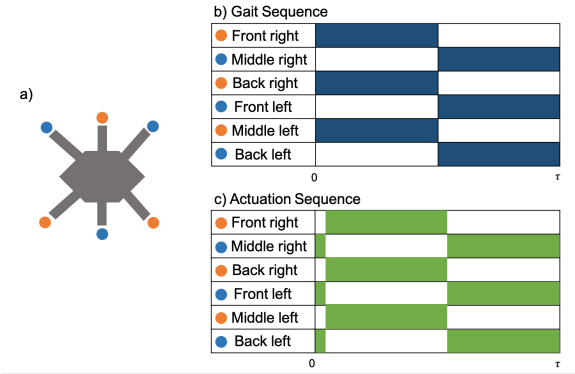

Figure 2.5: Gait Sequence. a) Hexapod top view. Motion is from left to right. b,c) Actuation and gait sequences for one cycle of the hexapod gait. The shaded region corresponds to when the foot is in contact with the ground. The shaded region in the actuation sequence corresponds to when negative pressure is drawn. The non-shaded region in the actuation sequence corresponds to positive pressure.

2.4.1 Speed Benefit

Jamming of granular feet can occur from passive effects such as weight being applied to the foot, and active control of the internal pressure. In order to quantify the effect of both passive and active jamming, we measured walking speed with a tripod gait over flat ground, wood chips, and loosely packed rock of diameter approximately 2/3 the size of the foot (N = 5 for all trials). For all trials, the hexapod carried the on board pumps and custom controller.

The first qualitative observation that we noticed between the feet with no reinforcing structures and the fiber reinforced feet was that the fiber reinforcement reduced failure in shear at the interface of a foot's bottom surface (ankle) and the jammed granular substrate. An image of

the base granular foot failing in shear is seen in Fig. 2.4b. This type of failure was not seen in the tests conducted with the fiber reinforced foot (Fig. 2.4c).

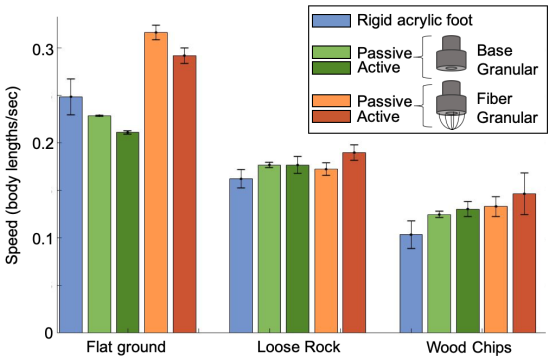

Figure 2.6: Speed of each type of foot in body lengths per second over flat ground (concrete), loose rock, and wood chips.

As seen in Fig. 2.6, on flat ground we see a statistically significant speed improvement between the rigid and base granular feet compared to the fiber granular feet, in both the passive and active cases (one-way ANOVA, F = 99.3), with the largest speed increase seen using the passive fiber reinforced feet. Over loose rock and wood chips, we see a statistically significant increase in speed from a rigid foot to the active base granular foot, and both the passive and active fiber reinforced foot (one-way ANOVA, F = 9.81, 7.48 respectively). We also see moderate increases in speed between the base granular design and the actively jammed fiber reinforced design.

We see that over both flat ground and loose terrain such as rocks or wood chips, granular feet enable benefits in walking speed, with the choice of passive versus active jamming determined by terrain type. We see that over smooth, flat ground passive jamming fiber reinforced feet perform the best, likely due to the ability to create a large and stable surface area of contact, as well as reduce energy loss at collision. Over loose rock (average diameter = 1cm) and wood chips, fiber reinforced active jamming feet perform best, likely because these feet are able to fill gaps in the substrate in their soft state and then jam, creating a stable foothold and reducing slip at the

interface between the robot and the substrate. We also see qualitative increases in the longevity the fiber reinforced design as compared to the base design, due to a reduction in shear failure (as seen in Fig. 2.4b).

2.4.2 Duty Cycle Necessary to Reach Desired Foot Trajectory

We next looked at how granular jamming feet can reduce the time it takes for the robot to reach its desired foot trajectory during a step. We measure the duty cycle of the motors during the gait to determine how much time the servos took to correct themselves and reach each desired foot trajectory during a step on both flat and irregular terrain. We define the duty cycle to be time to reach control stability over stance duration. Control stability is defined as servo position register error below 10.

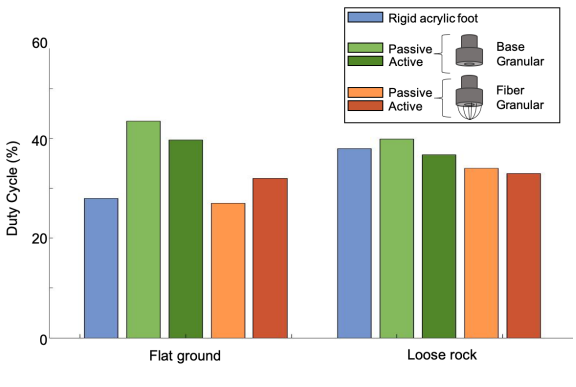

Figure 2.7: Motor duty cycle to reach desired foot trajectories over flat ground and loose rock.

In all cases, we see that the fiber reinforced granular feet are able to reach stability faster than the base granular design. On flat ground, active fiber reinforced granular feet take slightly longer to stabilize than passive fiber reinforced granular feet and rigid feet (avg duty cycle over more than 50 steps of 32% vs 27% and 28% respectively), but still perform better than the base granular design (45.5% and 40% for passive and active respectively) (Fig. 2.7). On loose rock, both passive and active feet help the robot reach its desired foot trajectories faster than rigid feet or the passive or active base granular feet (34% and 33% vs 38%, 40%, 36.8% respectively).

We see that adding compliance to the foot provides an advantage over loose terrain, but active jamming only provides a slight advantage compared to passive jamming. We also find that adding compliance does not hurt robot performance on flat ground, since leaving the foot in the passive conformation results in similar stabilization duty cycles to rigid feet. This suggests that granular jamming feet should be used in all terrain types in order to minimize duty cycle, with the choice of passive versus active jamming determined on a terrain by terrain basis. We also found it interesting that active jamming takes the same duty cycle on flat and loose terrain, which could have potential to simplify robot control in the future.

2.4.3 Maximum Net Thrust

The final performance metric we explored was the maximum net thrust that the robot with attached feet was able to produce over various natural terrains. Drawbar pull tests are often used to determine an exploration vehicle's maximum net thrust over loose terrain [49] and can allow us to quantify the performance limits of our feet.

We measured maximum traction force by attaching a linear elastic element (TheraBand) to the back of the robot and fixing the other end, then allowing the robot to walk forward until it reached the limits of its load pulling ability (Fig. 2.8a. We then measured the change in length of the linear elastic element from fully extended with no stretch to fully extended with stretch (dx) caused by the robot to compute the maximum traction force that the robot could generate.

As seen in Fig. 2.8b, rigid feet were able to generate more traction force on flat ground than any type of granular feet (statistically significant with one-way ANOVA, F = 27.81). Over loose rock, all granular feet were able to generate more traction force than rigid feet (statistically significant with one-way ANOVA, F = 4.86), but all granular feet performed similarly to each other, regardless of internal structure or jamming. We hypothesize that this limit is set by the force at which the rocks slip internally among each other, causing loss of traction not related to the foot internally or the foot-rock interface. On wood chips, active fiber reinforced granular

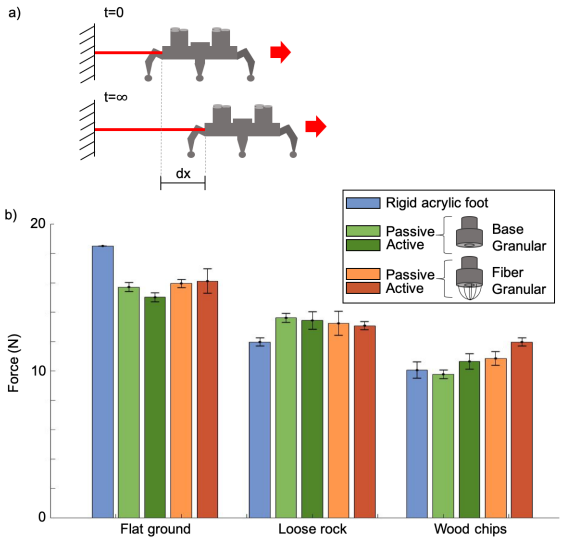

Figure 2.8: Drawbar pull test. a) Experimental setup with hexapod attached to a linearly elastic element, measuring change in length to determine force. b) Drawbar pull test results to measure maximum thrust over loose terrain.

feet were able to generate more traction force than any other type of foot (statistically significant one-way ANOVA F = 11.14).

In summary, over rigid terrain a rigid foot is able to generate more force compared to the granular jamming feet, which slip internally in their unjammed state, causing the robot to slip backwards when at its limits. Over loose terrain, granular jamming feet will increase a robot's traction, and therefore max net thrust, compared to rigid feet, due to the ability to create a larger area of contact with the uneven terrain, as seen in the results of the area of contact tests (Fig. 2.3). And in some cases, such as loose rock, the limit is determined by the substrate slipping on itself.

2.5 Conclusion

In this paper we hvae presented a new class of granular jamming feet for legged robot mobility. Our feet incorporate new internal structures that enable a hexapod robot to walk over varied terrain with lower control effort and larger traction force. The increases in robot performance are likely due to the ability of jamming feet to conform around obstacles and then to

become rigid, enabling a stable and high shear resistant foothold. We see that a granular jamming soft foot with abrasive fibers can still conform around obstacles, which is desirable, but can also increase it strength in shear, an important metric for walking. The results presented here highlight the performance benefits a robot can see with these new foot designs. The first two tests show the result for a single foot, and are generalizable to other legged agents. The tests on the hexapod test bench demonstrate trends that we believe would be similar in other legged robots.

We found it surprising that even a passively jammed foot imparts benefits in many situations, without need for actuation or control. In the case of flat ground, passive granular feet give the best results likely due to the ability to create a large and stable surface area of contact, as well as reduce energy loss at collision. In cases where the ground is likely to shift underfoot (e.g. loose rock), it is advantageous to have a passive foot that remains soft for the whole gait cycle so that the foot can re-adapt to the terrain underfoot as the terrain shifts within a step. In cases where the ground is rough but does not shift (e.g. wood chips), it is advantageous to have a foot that lands in a soft state, conforms around the terrain, and then stiffens, grabbing on to the terrain and using it as a platform from which to push off.

This finding enables future work that can focus on minimizing control and actuation effort by selectively jamming the feet or leaving them passive based on the terrain. Passively jammed feet could greatly reduce the energetic costs of walking compared to the actively jammed feet, which require a running pump. Incorporation of soft sensors on the bottom of the feet would enable sensing of ground stiffness as the robot transitions between terrain types, which can allow active selection of foot stiffness to best suit the terrain. Improvements in low-cost legged robotic mobility can help robots gain access to currently inaccessible terrains and environments. Strategies that utilize active modification of the shape and mechanical properties of appendages are a promising route to improved mobility in open-loop, sensor deprived environments. Future improvements of granular jamming foot design coupled with specific control and activation strategies provide an exciting new direction for legged robot mobility.

Chapter 2, in full, is a reprint of the material ”Shear Strengthened Granular Jamming Feet for Improved Performance over Natural Terrain” as it appears in the 3rd IEEE International Conference on Soft Robotics (RoboSoft 2020). Lathrop, Emily; Adibnazari, Iman; Gravish, Nick; Tolley, Michael T., RoboSoft 2020. The dissertation author was the primary investigator and author of this paper.

Chapter 3

Embodied Intelligence in Leg Design Enables Crevasse Traversal in Small Ground-based Robots

3.1 Introduction

To successfully deploy in natural environments, mobile robots need to traverse both open and confined spaces as well as transition between terrain types. In recent years, mobile robots have become increasingly capable of navigating in and around open natural spaces such as grassy fields, forest underbrush, and steep hills [5, 50, 51, 9, 52, 4]. In confined spaces, novel robot designs such as snake-like bodies [53, 54], limbs with compliant elements [55], or robots that use limb-wall interactions to their advantage [56] have been used to navigate tunnel environments and complete tasks such as pipe inspection or tunnel traversal [57]. But so far, less focus has been given to designing versatile robots that can seamlessly transition between various types of natural environments without the addition of many degrees of freedom.

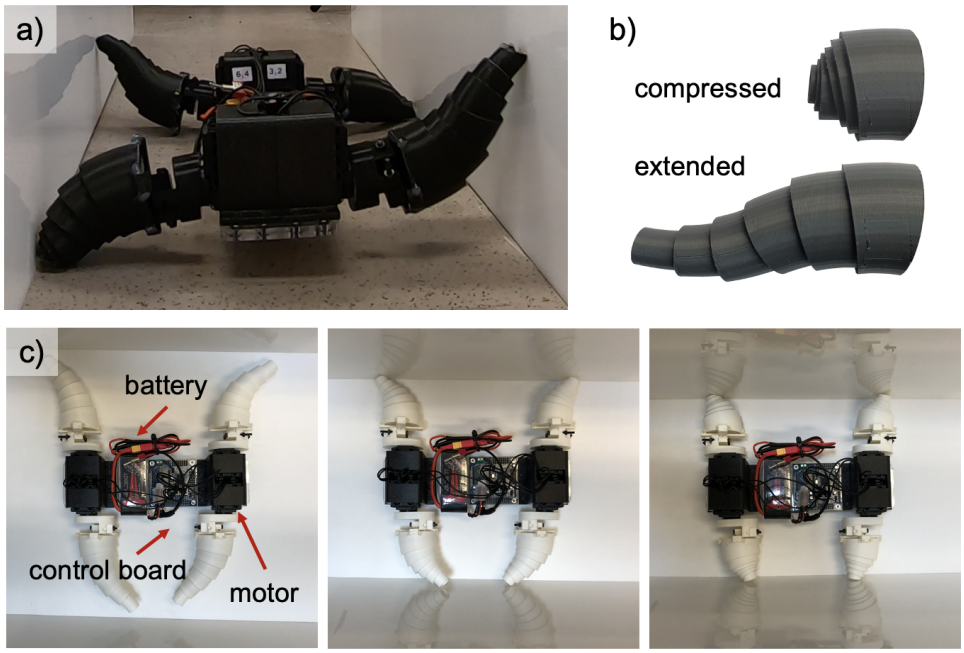

Figure 3.1: Robot with passively telescoping legs. a) Robot walking between two flat walls. b) Internal structure of a single leg consisting of 3D printed leg segments with internal springs. c) Robot system consisting of an on board battery, control board, and four continuously rotating motors. Robot with telescoping legs fully extended, partially compressed, and fully compressed in a channel.

When examining classes of mobile robots and the spaces they are designed to move through, we observe that most current mobile robots are designed with a particular environment in mind. Their morphology is then optimized around moving through that particular environment. As a result, they do not perform well when placed in other environments. For example, wheeled robots perform best on smooth, low roughness surfaces, and cannot traverse large ground obstacles [58]. Insect-scale compliant robots can navigate small spaces and tunnels but cannot move over human-scale terrain or obstacles much larger than their body size [59]. Robots with rigid limbs use feedback control to walk and run over unstructured natural terrain, but cannot compress to enter small spaces.

In order to create the next generation of versatile exploratory robots that can enter and move about in previously un-mapped spaces, new robot designs will need to be able to adapt to environments that can change as they move through them. This can include transitioning between unstructured terrain and confined spaces, moving quickly through many types of natural environments, and negotiating confined spaces where the geometry of the space changes spatially, such as a natural tunnels.

Our work was inspired by biological examples of animals that can move robustly through a wide variety of spaces, such as ants and cockroaches. One strategy that insects often use to navigate obstacles and fit into small spaces is to modify their effective width and height. This phenomenon is seen in ants as they tuck their legs under them to climb through narrow passages [60]. It is also seen in sandfish lizards, which reduce their effective width by tucking their legs into their sizes when moving through sand [61]. Many animals in nature also use body compliance to squeeze through constrictions. Common examples include octopuses squeezing through small holes [62] and cockroaches squeezing under doors [56]. In robotic contexts, other work has shown that embedding compliance into robot bodies can increase robot stability [5, 63] as well as increase the range of spaces robots can access [56]. All of the above examples make use of embodied intelligence, the coupling between an agent and it's environment through

body, perception, and system design constraints [20], to reduce control and actuation complexity through body design.

Our robot appendages were inspired by previous work on ant locomotion in tunnels, where it was found that in unconfined environments, ants use a wide, sprawled posture, but when compressed in tunnels, they narrow their sprawl and shorten their effective leg length by drawing their legs under their bodies [60]. We implemented these design principles in a robot system through the use of telescoping appendages, which achieved the same sprawl and leg length modifications that we see in ants, but through different mechanisms.

We demonstrate that our compliant appendages allow a robot to passively squeeze into small tunnels and under low ceilings and enable locomotion in confined spaces without sacrificing fast and stable locomotion in natural environments. In this work, we present the design of a telescoping leg robot that enables versatile movement in confined spaces (Figure 3.1a). Our robot can passively compress in response to environmental constrictions and shrink its effective body width and height through the use of collapsing leg segments (Figure 3.1b). We demonstrate that these appendages allow a robot to passively squeeze into small tunnels and under low ceilings and enable locomotion in confined spaces without sacrificing fast and stable locomotion in natural environments.

3.2 Background

Current metrics of success for mobile robots deployed in the wild are often evaluated through demonstrations across various types of natural terrain, as well as ability to traverse large obstacles, often quantified as maximum step height a robot can traverse as a function of hip height [59]. In a similar vein, in Figure 3.2 we seek to quantify existing robots on performance in confined spaces, defined as ability to modify body cross section to fit into constrictions of varying dimensions. Figure 3.2a demonstrates the maximum possible height and width compression that

current mobile robots are able to achieve relative to the robot's free standing dimensions. For example, a 30% width compression means that the robot can decrease it's body width by 30%, resulting in a body width that is 70% of the free standing body width.

3.2.1 Robots in Confined Spaces

Current robots employ several methods to navigate confined spaces that are smaller than their geometry would normally allow. One solution available to robots with a large number of degrees of freedom (DOF) is to re-position joints and limbs to enact maneuvers such as crouching or drawing limbs in from sprawled to more compressed postures [64, 65, 66, 3, 51, 67, 52]. But, modifying body cross section in this manner can be slow and computationally intensive. Other mobile robots circumvent this by taking advantage of body compliance [5, 56, 68, 69] to passively squeeze into small spaces. Some examples include flexible shells to squeeze under low ceilings [56] and flexible legs to squeeze through small gaps [18]. This type of strategy falls in the general category of embodied intelligence, where the mechanism for body shape change in response to environmental conditions is embedded into the body of the robot. This approach can allow robots to use simple, open-loop strategies to passively adjust to variable terrain features without the need for complex sensing or control [63].

In Figure 3.2a we show the maximum body compression along the largest body dimension for many popular mobile legged robots [5, 68, 70, 56, 71, 18, 65, 67] (see supplementary Table S1 for details). Although points in this plot capture the limits of possible shape change, it lacks nuance as to actual achievable robot geometries by making the assumption that a robot body is a compressible volume and height and width compression can be achieved independently. Functionally, this is often not the case.

To further estimate how legged robots can adapt to different confined volumes we make a constant volume assumption for their body reconfiguration capability. We assume that as body height decreases to accommodate lower height confines that the width must increase accordingly.

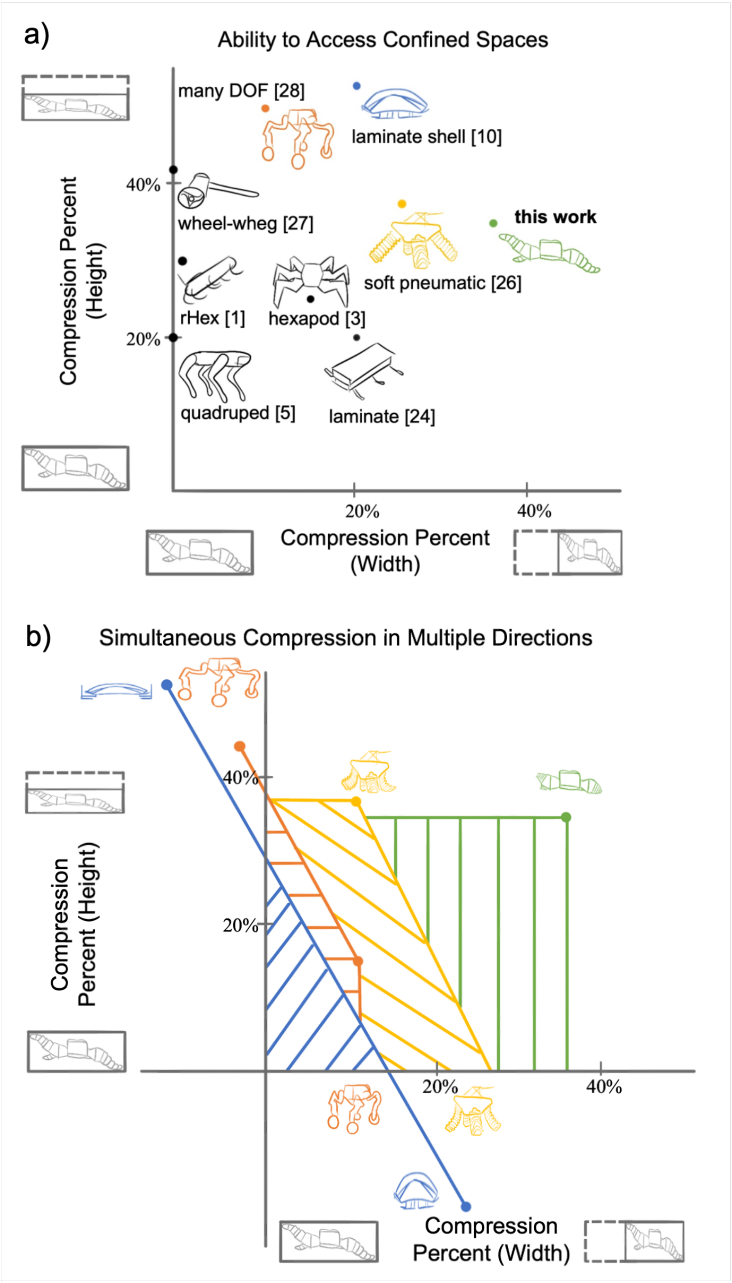

Figure 3.2: Current landscape of legged robot locomotion in confined spaces (See Supplemental Table S1 for details). a) Classes of mobile robots graphed on ability to modify body width and height to enter a confined space. Axes display maximum possible body height or width compression as a percentage of free standing robot height and width, where larger means able to compress more in that dimension. b) Achievable geometries for four classes of robots. Positive values correspond to body compression and negative values correspond to body expansion. Points in the shaded regions represent achievable robot geometries, as well as tunnel cross sections that each robot can produce a valid geometry to traverse.

In Figure 3.2b we show results from this analysis for four representative robot platforms. We observe that in all cases there is a trade-off between accommodating height and width confinement due to the constant volume nature of many legged robots (Figure 3.2b blue, red and yellow curves).

When plotting robot compression, positive values correspond to decreasing a dimension of a robot body and negative values correspond to expanding a dimension of a robot body. Points in the shaded regions correspond to robot geometries, as well as the cross-sectional dimensions of tunnels that each robot can traverse with an appropriate change in geometry. Using this method, one can evaluate the range of confined spaces that a robot can access and move within. These observations demonstrate the need for compressible volume robots and robot appendages that can compress in one dimension without expanding in another.

3.3 Design

3.3.1 Leg Geometry

Our robot appendages featured a telescoping design inspired from work done on concentric tube actuators [72, 73, 74]. This design enabled leg compression without expansion in another dimension by allowing the leg to collapse into itself. Our appendages differed in form and function from other concentric tube designs [75, 76] by the addition of internal springs between each leg segment. This allowed the appendages to support the robot body weight with minimal spring (and thus leg) compression. To maximize free standing body height, we attached the appendages to the robot body in an orientation such that the internal springs were primarily pointed in the horizontal direction, minimizing spring compression in the vertical direction that would occur due to the robot's body weight. We hypothesized that there existed an optimal leg spring stiffness that was low enough to allow passive compression when interacting with narrow walls but also high enough to support the weight of the robot without collapsing inwards.

The leg surface geometry was created in Unity using an open source design tool [74].

Using this tool, we created a six segment nested telescoping structure that followed the path of a cubic Bézier curve (Figure 3.3b). Each segment consisted of a hollow cylinder of decreasing radius with two guiding grooves running along the inside of each cylinder to inhibit rotation between segments. We adjusted parameters such as leg curvature, leg segment taper rate, wall thickness, and gap width between leg segments in order to fabricate legs that would telescope smoothly into each other with minimal friction between segments.

Each segment was held into the leg assembly by a lip at the proximal end of the cylinder. A flat plate was press-fit into the end of each cylinder, and a spring attached to each flat plate. Each spring faced internally into the body of the cylinder (Figure 3.3a). These spring spanned from flat plate to flat plate and were compressed when the legs telescoped in to each other.

3.3.2 Leg Fabrication

The segments and end caps were printed individually out of Acrylonitrile Butadiene Styrene (ABS) on a commercially available 3D printer (Prusa Research). During the printing process we tailored various parameters for the specific printer model and filament material so that the segments would nest tightly to reduce deflection in directions other than along the length of the spline. Printing parameters were also tuned to minimize friction between pieces to allow the leg segments to telescope smoothly into each other. These parameters included taper angle of each segment, gap width between consecutive segments, and the size and shape of the internal guiding grooves.

Once printed, the spring-caps were assembled by gluing one end of each of the five springs to one face of each of the five largest end caps. An exploded view of the leg components can be seen in Figure 3.3a. The leg was then assembled sequentially starting from the smallest segment by press-fitting a spring-cap into the distal end of the segment followed by inserting the segment into its next larger neighbor and repeating the process until all segments were assembled. The fully assembled leg can be seen attached to a robot in Figure 3.1a.

3.3.3 Robot Platform

Our robot platform consisted of four telescoping appendages mounted to four high torque servo motors (Dynamixel series). The robot was controlled via an Arbotix-M board and powered by an on-board Lithium Polymer (Li-Po) battery. The motors, control board, and battery were mounted to a flat plate of laser-cut acrylic, which served as the robot backbone. The robot used a continuous angular rotation diagonal coupled gait. The full dimensions of the robot platform were 26 cm in width, 20 cm in length, and 7.75 cm in height.

3.4 Modeling and Simulation

3.4.1 Leg Model

To predict the passive compression abilities of an appendage, we created a model of the motion of a single leg interacting with obstacles. The goal of the model was to determine how changing leg shape affected the passive compression ability of the legs. We first modeled a single leg interacting with a side-wall in order to predict the passive compression behavior of the robot walking through a narrow channel.

The fully extended leg is modeled and defined by a cubic Bézier spline with control points P_0 through P_3. To create the leg segments the spline was subdivided into six segments. The spline was defined as

$$\tilde{B}(t) = (1-t)^3 P_0 + 3(1-t)^2 t P_1 + 3(1-t)t^2 P_2 + t^3 P_3, t \in [0,1]$$

Each gait cycle, the motor rotated the leg by θ around the motor axis x to give leg position:

$$\tilde{B}(\theta,t) = R_x(\theta)\tilde{B}(t)$$

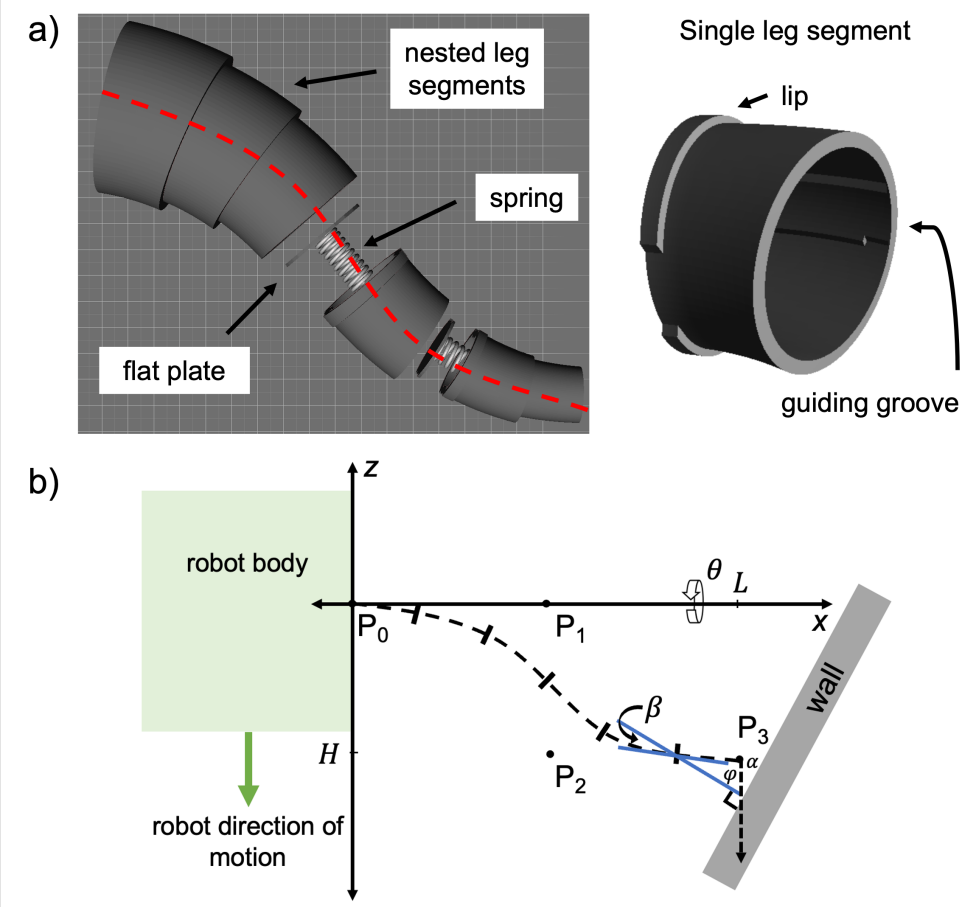

Figure 3.3: Leg design and model. a) Internal structure of a single leg consisting of 3D printed leg segments with internal springs attached to plates located at the end of each leg segment. Leg is assembled sequentially. b) Top down view of a leg interacting with an angled wall where P_0 through P_3 are control points for the Bézier spline that defines the leg, θ is the angle by which the leg rotates around the hip joint, L is the width of the leg, H is the height of the leg (hip height), α is the angle of a wall with respect to the robot direction of motion, $\phi = 90 - \alpha$ is the wall normal, and β is the angle between the leg spline tangent and *phi*.

where $P_0 \rightarrow P_3 \in \mathbb{R}^3$ were spline control points originating in the xz plane with P_0 = [0,0,0] in the base of the leg frame (Figure 3.3b).

As a leg encountered a flat wall obstacle positioned at angle ϕ with respect to the robot direction of motion (Figure 3.3b), a side-wall normal can be written as $N(x,y,z) = (\sin\phi, 0, \cos\phi)$ and a ground-normal can be written as $N = (0,1,0)$. The angle β between the tangent to the leg spline and the normal to the wall was used to determine the component of force causing spring compression in the leg.

$$\cos\beta(\theta,t) = \left| \frac{B'(\theta,t) \cdot N}{|B'(\theta,t)||N|} \right|$$

When the robot moved forward in a channel, the force compressing the internal springs is the component of the traction force pointed in the direction of the leg spline. This force is written as

$F_c(\theta) = T\cos\phi\cos\beta$ where $T = mg\ \tan(\mu)$ was the traction force generated by the robot while walking, μ was the friction coefficient between the robot leg and the ground, and m was the mass of the robot. The forces opposing leg compression were the sliding friction between the segments $F_f(\theta) = T\cos\phi\sin\beta$ and the spring's restoring force.

We used this model to calculate the leg length change of each segment caused by the compression force described above as a leg interacted with a wall of angle ϕ. During a cycle, passive leg compression was maximized when $\theta = \frac{3\pi}{2}$ which corresponded to when the leg was pointed forward (in the xz plane).

3.4.2 Walking Robot Simulation

To determine the optimal spring stiffness for the springs inside the telescoping legs, we simulated the robot traversing two high walls of varying width and swept through a range of spring stiffness values, observing the resulting speed of the robot through the channel (Figure

3.6a). The variance between trials can be accounted for by varying the initial phase of the robot legs between simulation runs. We used a simulation environment tailored to robotic systems (CoppeliaSim) running a popular rigid body dynamics solver (Bullet 2.78). The spring-mediated telescoping action was simulated by attaching virtual prismatic joints in spring-damper mode between the leg segments. In the simulation, we set the sliding friction between leg segments to zero in order to more closely examine the dynamic robot behavior and the interactions the robot legs had with their environment, eliminating the within-leg interactions seen in the analytical model above.

3.5 Results

3.5.1 Model Fitting

After developing a leg compression model that accounted for internal friction, we investigated how modifying parameters such as leg stiffness and leg shape could minimize the force needed to compress the legs across a range of channel angles. We first measured the force-displacement compression curves of 3D printed appendages using a motorized test stand (Mark-10 ESM750S, Figure 3.4a). We then used these curves to estimate a lumped parameter value for the friction coefficient μ_s between leg segments ($\mu_s = .75$). This parameter accounted for fabrication-induced friction such as layer roughness and print direction. Using this value, our model matched experimental curves for both a very stiff leg (k = 500) and an optimal stiffness leg (k = 250) interacting with a representative wall of angle $\alpha = \pi/6$ from parallel (Figure 3.4b).

3.5.2 Optimal Leg Shape

After matching our model to experimental curves, we investigated the effect of spline shape on the passive compressive ability of the telescoping legs while the robot is inside a channel.

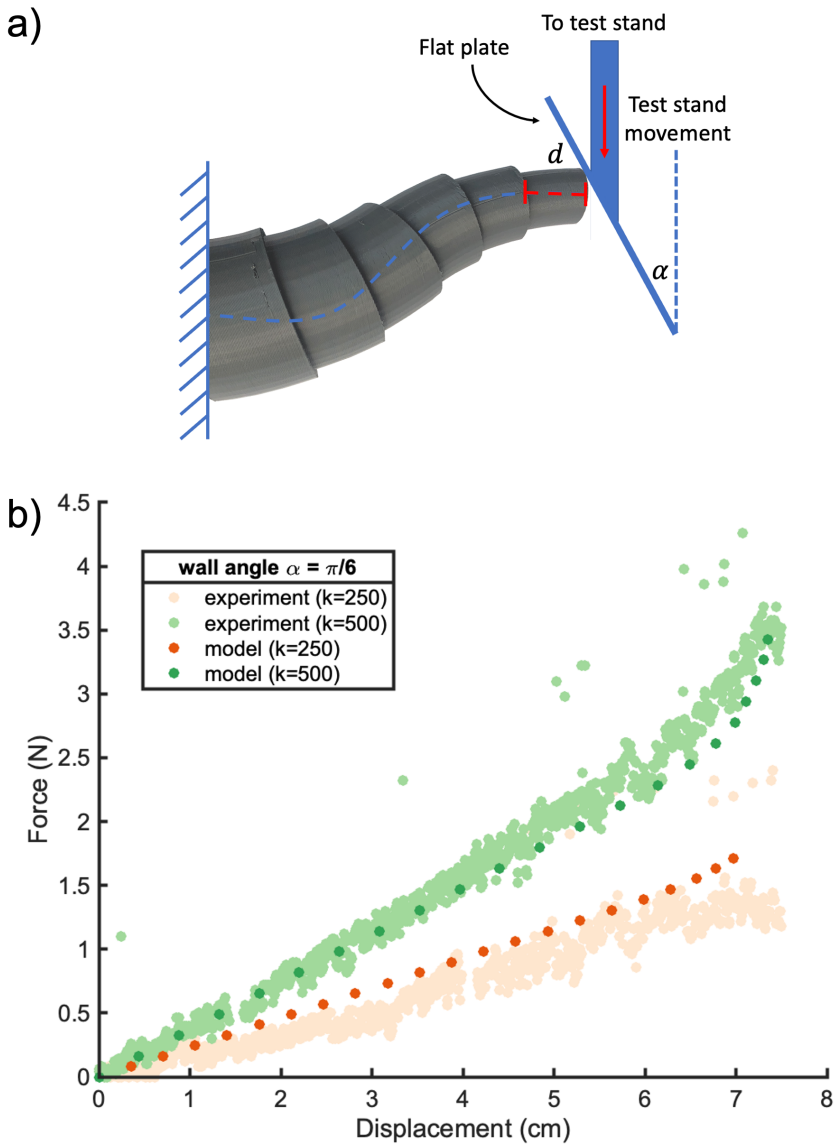

Figure 3.4: Force vs. displacement test on a single leg. a) Force displacement test setup. b) Force displacement tests were performed on telescoping legs of two stiffnesses in order to determine a lumped parameter value for the model that describes the friction between leg segments within a leg.

We examined how the maximum leg compression varied as the spline shape changed with the goal of choosing a leg shape that would offer high passive compression when it encountered walls of a wide range of orientations with respect to the leg.

We found that the passive leg compression in both the horizontal and vertical directions was dependent on the shape of the spline and that the optimal shape consisted of a spline with control points $P_0 = (0,0)$, $P_1 = (L/2 - 1.46, 0)$, $P_2 = (L/2 + 1.46, H)$, and $P_3 = (L, H)$ (see Figure 3.5a and 3.5b). A spline with these control points achieved a passive width compression of on average 82.4% of the compressible length of the leg (Figure 3.5a) and a height compression of 79% (Figure 3.5b) when walking through channels with contact wall angles ranging from 0 (parallel) to $\pi/4$ radians. We found that leg compressibility varies depending on the angle of the channel walls (Figure 3.5c, d).

3.5.3 Optimal Leg Stiffness

We next used simulation to determine the optimal stiffness for the springs embedded in the legs. We simulated how varying the stiffness of the springs between leg segments effected the walking speed of the robot inside a channel. Intuitively, we expected the optimal spring stiffness to be a balance of a high enough stiffness to support the weight of the robot, but also a low enough stiffness so that the legs would compress when confined in a channel.

In the simulation, the robot began in open flat ground and then was funneled into a narrow channel. Channel widths were varied from 100% robot body width (legs were completely uncompressed while walking in the channel) to 70% robot body width (legs were compressed 30% while walking in the channel). We then measured the time to traverse the channel to obtain robot walking speed in the channel (Figure 3.6b). We varied the starting phase of the legs between trials, which is reflected in the error bars in Figure 3.6b.

Our simulation results showed that the optimal spring stiffness for maximizing robot speed in a channel was dependent on the width of the channel (Figure 3.6b). We averaged performance

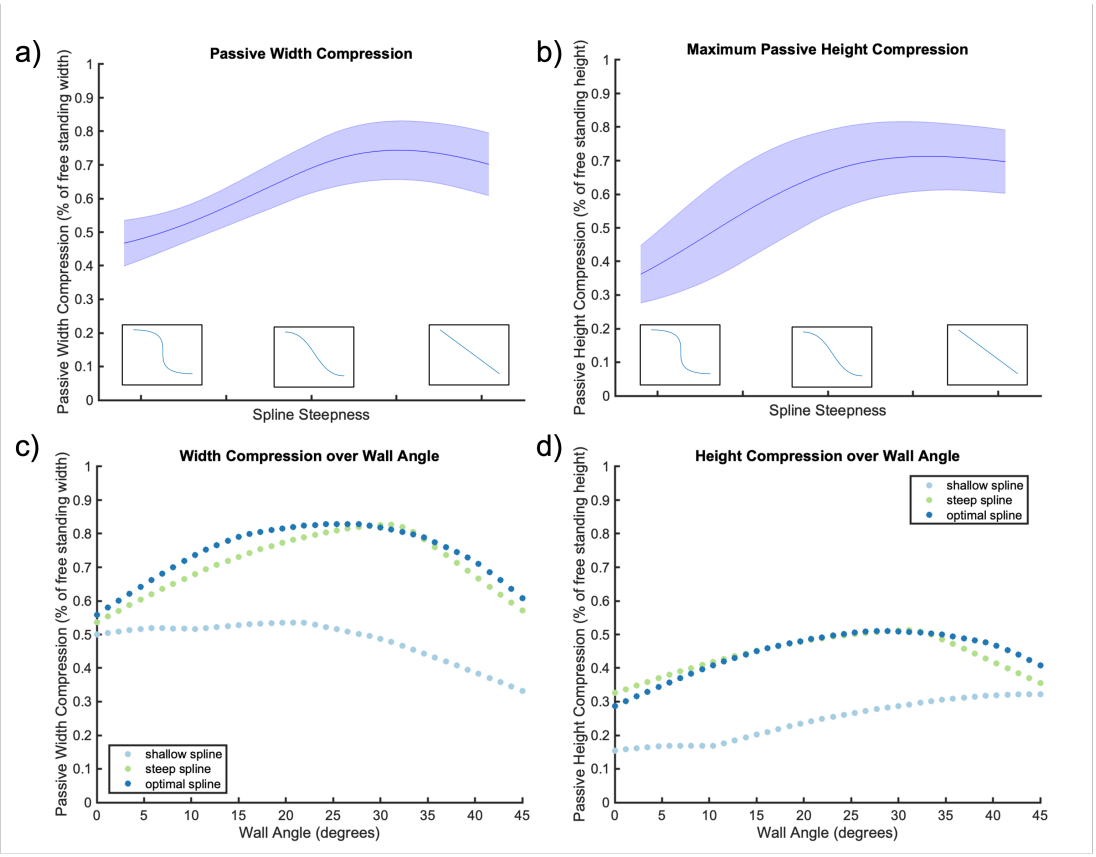

Figure 3.5: Maximum achievable passive leg compression when interacting with walls over a range of spline shapes. a) Maximum leg compression in the horizontal direction that can be achieved passively by the force of the robot leg hitting a wall varies as spline shape varies. Representative spline shapes are shown along the axis. Line and shaded region correspond to the average and standard deviation for maximum leg compression over over walls ranging from 0 to $\pi/4$ rad. b) Maximum leg compression in the vertical direction that can be achieved passively, averaged over a range of wall angles. c) Passive width compression varies depending on the angle of the wall the limb is interacting with and the shape of the spline. d) Passive height compression varies similarly.

over a range of moderately narrow channels (70% to 90% of the unconstrained robot width) and chose a spring stiffness of k = 250 to implement on our robot platform.

3.5.4 Leg Stiffness Validation on Robot Platform

We attached legs of various stiffnesses to our experimental platform and showed that the optimal stiffness legs performed best in a wide range of scenarios. We fabricated three robot platforms: one featuring telescoping legs with no springs, one with internal springs of the optimal spring stiffness found in simulation (k = 250), and one featuring stiff springs (k = 500). We compared walking performance of these three robots through a channel formed from two vertical acrylic plates and found that, over a wide range of narrow channels, the robot with the optimal spring stiffness was able to walk faster than the robot with stiff internal springs (Fig. 3.7a), with exception of unconfined walking, where the speed was similar. The large speed decrease in the stiff legs can be explained by the intuition that if one forces a leg with very stiff springs to compress a large amount, the restoring force results in the legs jamming themselves between the walls, hindering progress.

The robot equipped with legs with no internal springs resulted in each leg fully collapsing into itself, resulting in what was functionally a wheel composed of the largest leg segment. The length of these legs were not variable, and their speed was constant and dependent on wheel radius. Although these wheel-legs resulted in a narrower overall body width, they were not able to achieve the same maximum speeds as their legged counterparts in less confined spaces (Figure 3.7a). Additionally, these wheel-legs were unable to navigate tall steps or natural terrain with large features.

3.5.5 Speed Dependence on Leg Length

Robot walking speed is a function of stride length and stride frequency. On this robot platform, stride length was directly proportional to the hip height of the robot, which was a

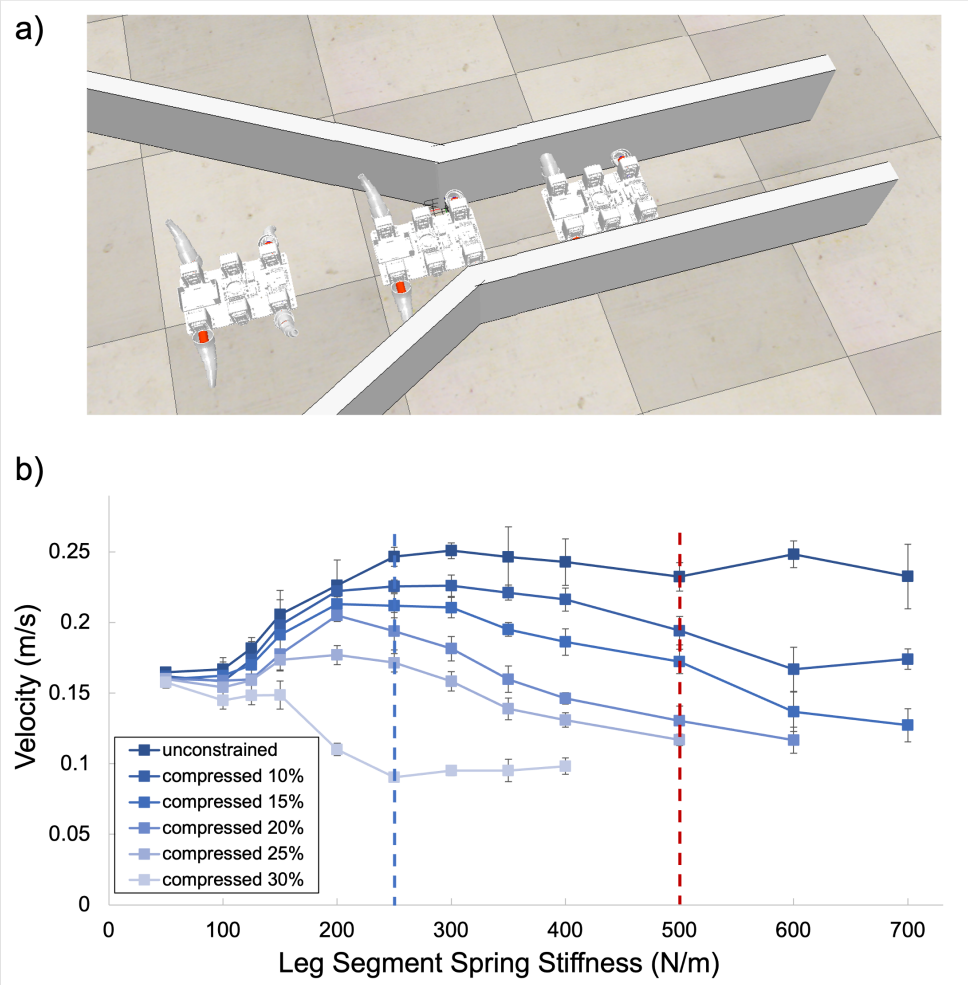

Figure 3.6: Simulation to determine optimal spring stiffness. a) Simulation setup in CoppeliaSim. b) Robot walking speed in channels of various widths and with legs of varying stiffness. Starting phase of legs was varied between trials (n=5). Dotted lines depict the stiffness values for the two legs tested experimentally: blue for the optimal stiffness case, red for the too stiff case.

function of leg length (Figure 3.7b). We experimentally validated the dependence of speed on leg length by fixing the legs in partially compressed positions and measuring walking speed over flat ground (N = 3). This relationship motivated the need for long but compressible appendages to maximize speed in open terrain yet still allow confined spaces to be accessible. The speed drop-off seen in confined spaces (Figure 3.7a) was also be explained by this relationship: narrow channels caused greater leg compression, which resulted in a speed that was proportional to that compressed leg length.

3.5.6 Robot Demonstrations

In the following section, we demonstrate that our robot is successful at navigating many diverse natural environments including confined spaces, steps, and rough ground. All trials were conducted with the robot platform and walking gait described in Section 3.3, with N = 3.

Entering and Traversing Narrow Channels

Our robot was capable of transitioning from free walking to entering an angled and narrowing tunnel narrower than the robot's body width (Figure 3.8a), and walked in both parallel and angled channels. Channel widths tested ranged from 25 to 35 cm in width and speed was measured over a channel length of 90 cm. The uncompressed robot width was 30.5 cm. At channel widths larger than 80% the robot was able to enter and walk inside with a success rate of 100%. The minimum channel width the robot was able to enter and walk through was 72% of the robot's uncompressed width, with a success rate of 50%. This was close to the theoretical limit of 65% of the robot's uncompressed width, which was determined by the total width of the rigid components of the robot body. We demonstrated that robot speed in these channels as a function of gap width agreed well with our simulation (Figure 3.7a), and the robot with the optimal leg stiffness walked faster than the robot featuring stiffer legs (Figure 3.7a).

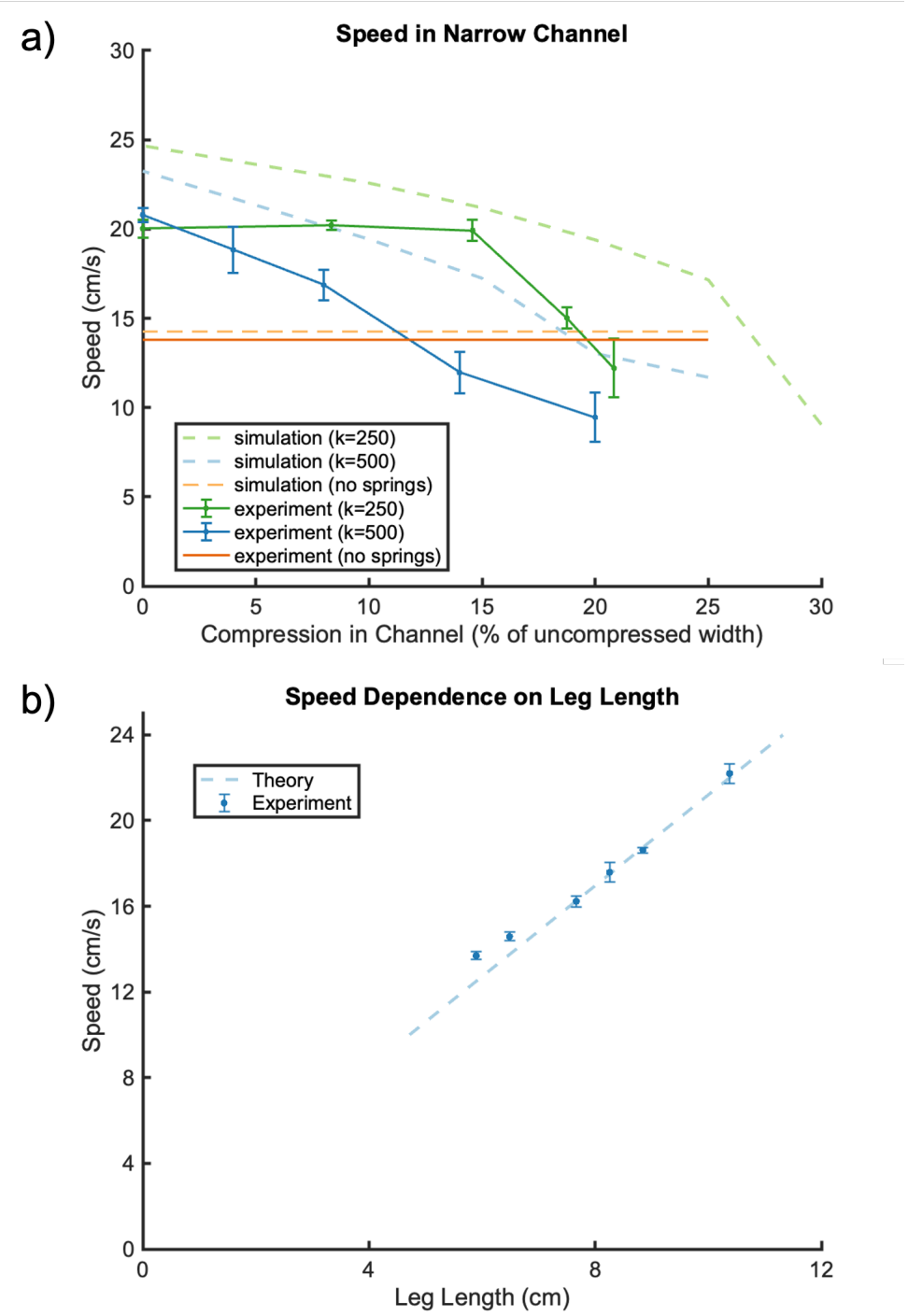

Figure 3.7: Robot walking speed in narrow channels. a) Speed versus channel width for a robot equipped with spring legs of optimal and non-optimal stiffnesses, as well as with telescoping legs with no internal springs, which fully collapse into the largest segment, creating a consistent, wheel-like rolling motion with the largest segment serving as a wheel. b) Speed over flat ground is dependent on leg length. Legs were constrained to a length and then robot speed over flat ground was measured (N = 3).

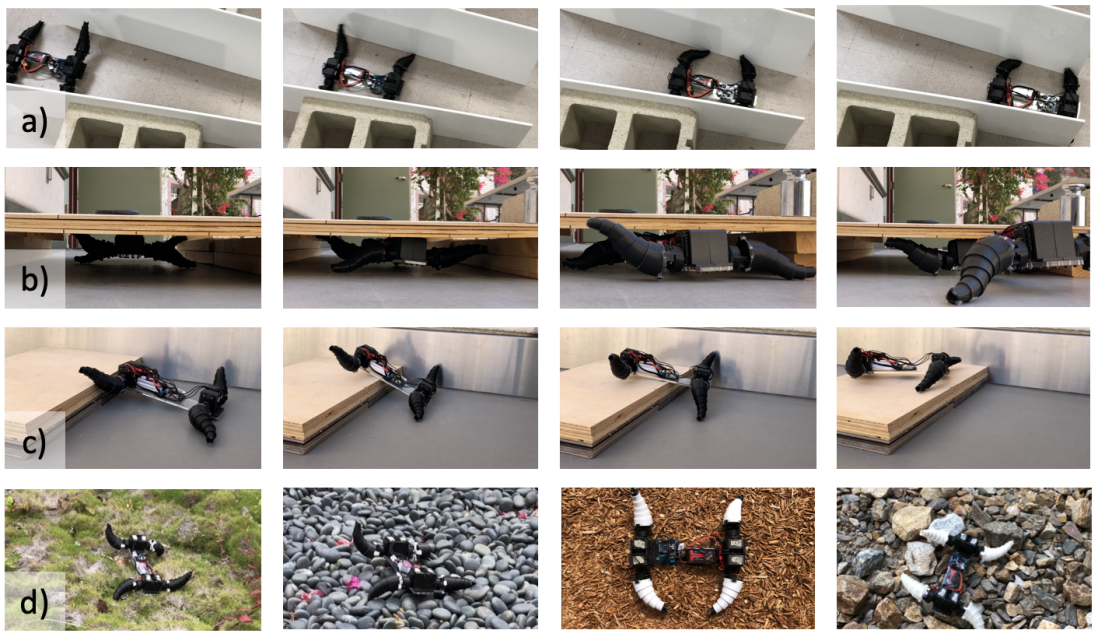

Figure 3.8: Robot in the wild. a) Demonstration of robot walking between narrowing walls whose minimum width is 72% free standing body width. b) Demonstration of robot walking under a low ceiling 68% of free standing height. c) Robot climbing over a step (1.6x hip height). d) Robot walking over unstructured terrain.

Squeezing Under Low Roofs

The robot legs were able to passively compress to squeeze the robot under a low roof that is 68% of free standing body height (Figure 3.8b) with an 100% success rate. This compression was in part driven by leg compression and in part driven by the driven by the pitch and roll motion of the alternating quadruped gait, which increased the amount the leg segments are pointed towards the ceiling during portions of the leg cycle, bringing β closer to parallel with the wall normal. Free standing robot height was 11 cm and the maximum height a leg achieved during each cycle due to the unstable gait was 14 cm.

Step Traversal

These appendages also performed well at tasks such as step traversal. Our robot reliably climbed onto and over obstacles 1.6x it's hip height (N = 5 with an 100% success rate), which is

consistent with existing legged robot traversal abilities [59].

Natural Terrain Locomotion

Our robot was also able to walk over various types of unstructured terrain (Figure 3.8d). The robot was able to walk through thick grass with a speed of 16.1 cm/s (N = 3) and over loose wood chips with a speed of 16.1 cm/s (N = 3). The robot was also able to work over both smooth and jagged rocks of sizes ranging from 1cm to 10cm in diameter with a speed of 14.8 cm/s (N = 3).

3.6 Conclusion

In this work, we presented the design of a telescoping appendage that allowed a robot to modify it's leg length in response to environmental constrictions without added actuation or power requirements. We have optimized the shape and stiffness of these telescoping appendages to maximize performance and have demonstrated that a robot equipped with these appendages can passively enter narrow channels and move quickly through them. We have also demonstrated that a robot equipped with these appendages successfully navigated natural terrain obstacles such as rough ground and tall steps.

In the future, active stiffness modulation between leg segments could help bridge the performance gap between high stiffness spline shapes (for flat ground) and high leg compression (when interacting with walls). This active control of stiffness for legged robots has been studied in works such as [77], [78], and [55]. Recent developments in soft robot design also present an opportunity to design robots with active stiffness control and infinite DOFs [79], however these approaches require onboard pumps and valves which come at a performance cost.

The appendages presented in this work offer exciting opportunities for translation to smaller scales, where manufacturing, powering, and actuating many DOFs becomes difficult.

Because of these challenges at a small scale, creating versatility through embodied intelligence becomes increasingly important. This is especially true since terrain experienced as smaller scales presents much more height variation and constriction, relative to body size, than terrain experienced by meter-scale walking robots. As a result, small scale robots need to be able to navigate large, cluttered obstacles with ease.

In this work we developed a collapsible leg that enables navigation of complex terrain using minimal control feedback. This embodied alternative to high DOF limbs can enable the design of smaller robots without sacrificing terrain adaptability or versatile movement. The ability for a robot to modify body size is useful when looking to deploy robots in environments with unknown features and obstacles such as cave systems or building rubble. In these situations it is often not possible to predetermine the types of obstacles a robot may encounter and it is advantageous to have a robot that can compress in one dimension without sacrificing compressibility in another. In the future, designs that use embodied intelligence to reduce actuation requirements can enable small but versatile robots to be deployed in applications such as search-and-rescue, disaster response, mapping of small interior spaces, and exploration in caves and tunnels.

Chapter 3, in full, has been submitted for publication as ”Embodied Intelligence in Leg Design Enables Crevasse Traversal in Small Ground-based Robots” as it may appear in Advanced Intelligent Systems. Lathrop, Emily; Tolley, Michael T.; Gravish, Nick. The dissertation author was the primary investigator and author of this paper.

Chapter 4

Local Fluidization of Granular Media for Directional Force Reduction in Digging Robots

4.1 Introduction

Subterranean locomotion through granular media requires overcoming large resistive forces. A method to potentially reduce these forces is to locally fluidize the surrounding media by controlling the flow of air or water through the media. Traditional digging approaches involve soil excavation to create free paths to move along. This method can be seen in industrial applications such as in augers and tunnel boring machines [80], as well as in nature in mole tunnels [81]. This process is slow and energy intensive, and not well suited for small-scale robots that cannot generate large forces against the soil. At a smaller scale, animals such as earthworms [82] and sandfish lizards [61] use wriggling and undulating (respectively) to move by locally compacting the material around their bodies [83, 84].

The multi-phase property of granular media enables a strategy for reducing the high forces that make digging in granular media so difficult [84]. While many traditional diggers such as excavators compact granular material and interact with it in solid-like states, smaller animals and robots will instead fluidize the material by disturbing the solid so that the material exhibits flowing, viscous-like behavior [29]. This reduces the forces needed to move through the material. Granular fluidization is seen underwater in animals such as the pacific sandfish or the sand octopus [84] and has also been used in drilling contexts [85, 86].

The main contributions of this work are as follows: 1) We present a method of creating bulk fluidization over large surface areas; 2) We characterize the physics and resulting forces this type of fluidization; 3) We show that fluidizing panels on the surface of an object can be used to directionally alter the forces an object experiences when moving in granular media; 4) We add a fluidization scaling factor to 3D resistive force theory (RFT) and show that we can successfully predict the forces on an object with fluidizing panels; and 5) we demonstrate how local fluidization can enhance subterranean locomotion in a digging robot.

4.2 Background: Fluidization in Granular Media

In the following section we describe the landscape of granular fluidization, differentiate between types of fluidization, and determine the parameters relevant for characterization the physics of uniform local fluidization.

Granular fluidization falls into a few categories dependent on the location of the flow source (static vs. mobile) and how localized the flow source is (local vs. bulk) [87]. Static fluidization refers to stationary setups consisting of a tank filled with granular media and fluidization that originates at the base of the tank. This setup has been employed widely in industrial applications such as mixing and drying and has also been used in robotic contexts to create uniform granular experimental platforms [88]. In contrast to static setups, mobile fluidization is where the flow

source is attached to a moving platform, such as a robot. Additionally, flow sources can be divided into either local sources, where the fluid input is concentrated into a small diameter jet and fluidization falls off sharply away from the jet [89, 87], or bulk sources [90], where the fluid input is spread over a large area.

Previous work has successfully used local mobile fluidization to design digging robots [91, 92, 93]. In all these cases, the flow source is is localized jet of liquid, which limits applicability to diggers with small cross sectional areas, since fluidization and the resulting force reduction drop off away from the jetting source [87]. In contrast, in the following section we use bulk fluidization, where the fluidization source is spread across large surface area fluidizing panels (Fig. 4.1a). By equipping mobile robot body surfaces with fluidizing panels, we can selectively alter drag across robot surfaces and enable drag reduction across large body surface areas. The focus of the following sections is to characterize the physics of uniform local fluidization and demonstrate how this method of fluidization can be applied to directionally alter drag forces in granular media.

4.3 Physics of Fluidization

According to resistive force theory (RFT), the force acting on a plate intruding in granular media are dependent on the orientation, direction of movement, and depth z of the intruder [88]. For a fluidizing sheet, the forces are also dependent on the mass flow through the sheet $\dot{m}$. By Fick's law, mass flow is proportional to the the pressure differential $P_2 - P_1$ between one side of the sheet to the other, the sheet diffusivity, ρ, the sheet thickness, L, and inversely proportional to the cross sectional area of the sheet, A.

$$\dot{m} \propto \frac{\rho(P_2 - P_1)A}{L}$$

4.3.1 Experimental Setup

In the following section we characterized the relationship between the parameters described above and the force felt by a flat-pate fluidizing probe as it was vertically intruded into a bed of granular media. The probe design consisted of a flat porous plate (Porex 4905) backed by a 3D printed funnel, which was attached to an air supply (Fig. 4.1a). Pressurized air flowed in to the backing chamber and was then diffused over the area of the porous sheet. We fabricated test probes of varying cross sectional areas (3 cm x 3 cm, 4 cm x 4 cm, 5 cm x 5 cm, and 6 cm x 6 cm) and varying sheet thicknesses (0.635 cm and 1.27 cm). The probe was attached to a linear stage with attached force sensor, which was mounted above the granular bed and vertically intruded the probe at a constant velocity into the bed at a speed of 3.1 cm/s, up to a depth of 7 cm (Fig. 4.1b). The test bed was filled with 0.3 mm diameter loosely packed glass spheres and had a fluidizing floor, which was used to reset the compaction of the material between trials.

4.3.2 Effect of Input Pressure

To examine the effect of input pressure on force, we intruded a 5 cm x 5 cm fluidizing sheet into granular media at a constant velocity, and plotted force over time (Fig. 4.1c). At $t = 0$, depth was 0 cm and at $t = 2.5$, depth was 7 cm. At an input pressure of 0 kPa, we saw a linear relationship between force and depth, consistent with previous literature [88]. At input pressures larger than 0 kPa, we saw a nonlinear relationship between force and depth that changed with input pressure, which was consistent with the literature on fluidization with jets [93]. Overall, increasing input pressure correlated with decreased force across all depths.

We then divided the force at each input pressure by the force at an input pressure of 0 kPa (no fluidization) and determined a scaling factor that could be used to scale down force as a function of input pressure and depth (Fig. 4.1d). This was then used as an additional factor on top of methods such as 3D RFT [94] in order to predict intrusion forces for fluidized intruders in

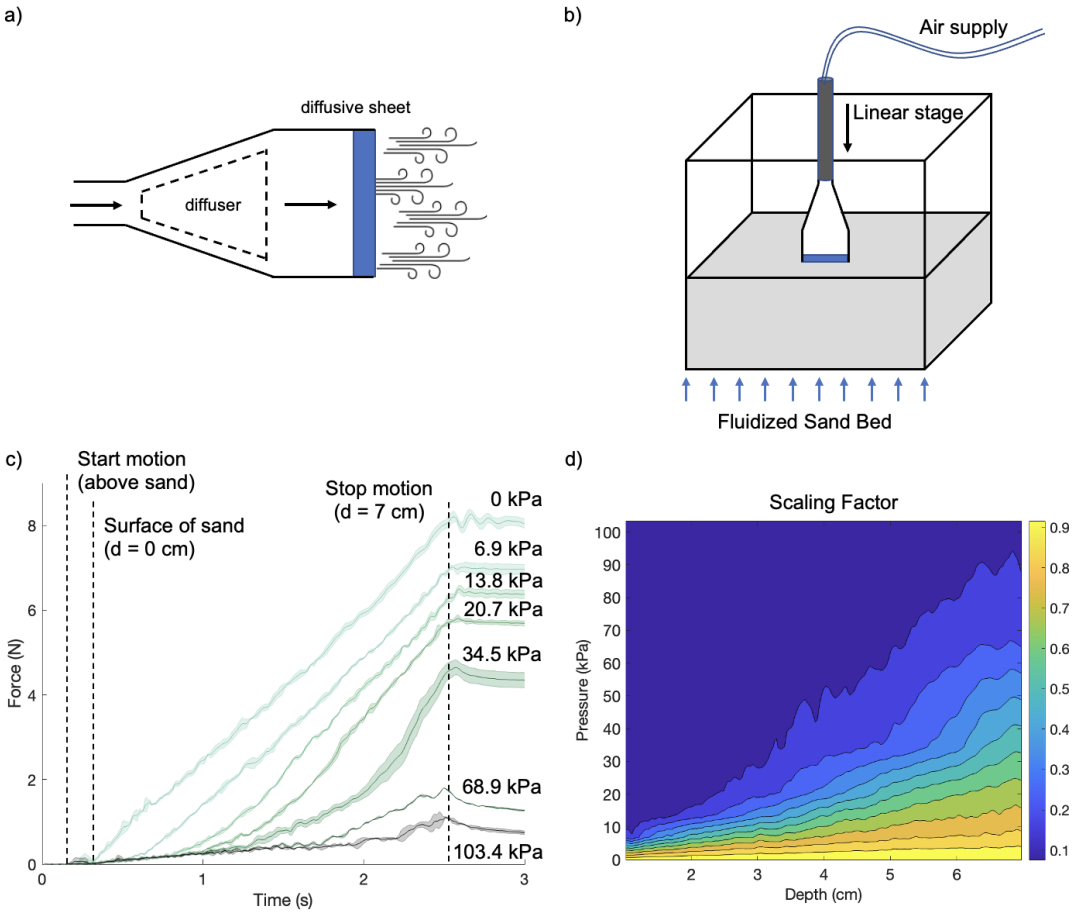

Figure 4.1: Vertical intrusion experiments on a diffusive sheet. a) Diffusive sheet backed by an air chamber and connection to external air supply. b) Experimental setup consisting of a flat-plate diffuser, fluidized sand bed, and linear stage. c) Force over time for diffusive probe as it intrudes into granular media. Force was found to be non-linearly dependent on input pressure and depth. d) Scaling factor for force as a function of input pressure and depth. Scaling factor was calculated by dividing the force curve at a pressure by the force at that depth for an input pressure of 0 kPa.

granular media.

4.3.3 Effect of Surface Area

We then examined the effect of surface area of the intruder on force. We performed vertical intrusion tests on fluidizing plates of surface areas of 3 cm x 3 cm, 4 cm x 4 cm, 5 cm x 5 cm, and 6 cm x 6 cm that were fluidized at an input pressure of 34.5 kPa (Fig. 4.2a). We found that force scaled with surface area squared (Fig. 4.2b), which can be contrasted to forces on non-fluidizing plates [88] and forces on intruders in partially fluidized static beds [95], which both scale proportionally to surface area.

4.3.4 Effect of Sheet Thickness

In the following test we examined the effect of modifying the thickness of the diffusive plate. Using the setup and experimental method described above, we again performed vertical intrusion tests but this time varied sheet thickness and held sheet surface and input pressure constant. The two thickness values tested were 0.635 cm and 1.27 cm. Testing was done on a 5 cm by 5 cm area plate at an input pressure of 34.5 kPa. We found that forces were slightly higher at larger plate thicknesses (Fig. 4.2c), which follows from the mass flow equation. When doubling the plate thickness, the magnitude of force increase was on the order of $1.1\times$.

The small change in force when doubling diffusive sheet thickness indicates that other sources of resistance, such as the resistance of the connecting tubing, are also present in the system.

4.4 Fluidizing Probe Attached to Robot Arm

Next, we examined how fluidization could directionally reduce forces on an intruder in granular media. We show that drag reduction is directional, and dependent on the orientation

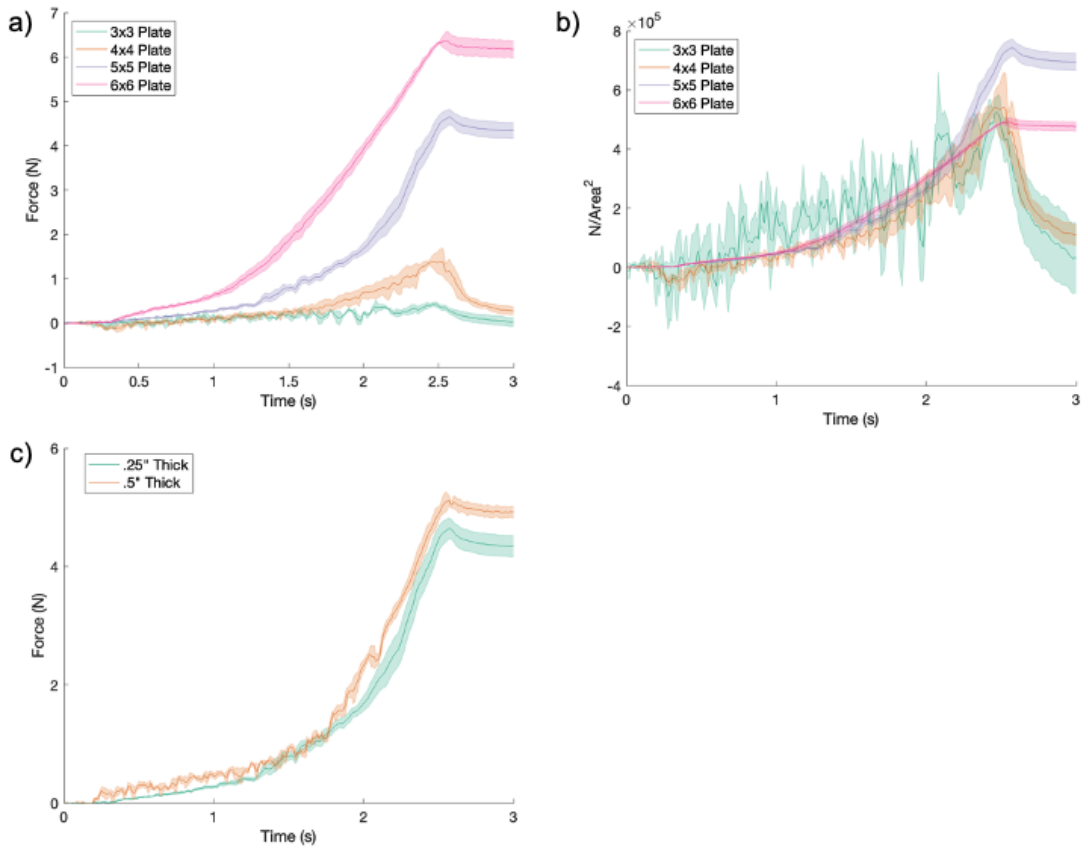

Figure 4.2: Effect of surface area and sheet thickness on force. a) Force profile for vertical intrusion test on fluidizing sheets of varying cross sections, all pressurized at 34.5 kPa. b) Force over area squared for the test in (a) shows that force scaled with area squared. c) Force curve for a vertical intrusion test for a 5 cm by 5 cm plate with varying thickness (0.635 cm and 1.27 cm) at an input pressure of 34.5 kPa demonstrated that the majority of the resistance of the system was due to the resistance in the tubing.

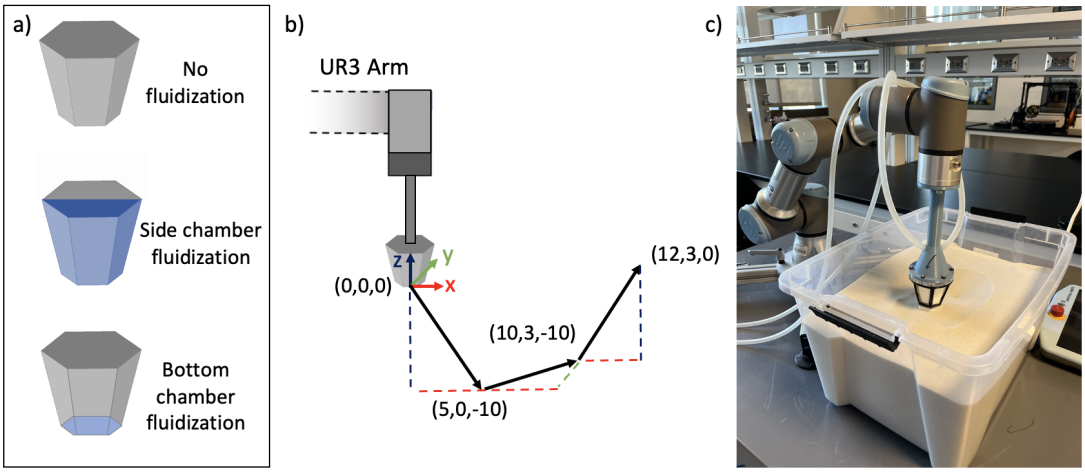

Figure 4.3: Fluidizing probe with independently fluidized surfaces attached to a robot arm. a) The side fluidizing surface was composed of three of the six panels that made up the walls of the probe, and pressurized by a single input source. The bottom fluidizing surface contained a separate backing volume and input source from the side panels. b) A robot arm moved the probe in a complex path through a bed of granular media. c) Picture of the experimental setup.

of the fluidizing surface and the direction of movement of the intruder. We designed a two-chambered fluidizing probe (Fig. 4.3a) that consisted of a 3D printed chamber with two internal cavities and connections to an external air supply. One internal chamber was connected to the bottom fluidizing panel and the other was connected to side panels which fluidized three out of six of the sides of the probe. The other three panels and the top of the probe were printed from non-porous acrylonitrile butadiene styrene (ABS). Each chamber could be fluidized independently or left un-fluidized.

This probe was then rigidly attached to a robot arm (Universal Robots UR3), which moved in a complex path (Fig. 4.3b) through a bed of granular material (0.3 mm glass spheres). Position and force along the path were recorded for no fluidization, bottom surface fluidization, and side surface fluidization. In all cases the chambers were fluidized at a gauge pressure of 34.5 kPa.

4.4.1 Vertical Force Reduction

For the setup described above, we examined the vertical (z) force as the probe traced a path with a vertical component followed by a horizontal component (Fig. 4.4) for three fluidization cases: 1) no fluidization, 2) side fluidization where the fluidizing surface was pointed orthogonal to the direction of motion (34.5 kPa), and 3) bottom fluidization (34.5 kPa). We found that forces were directionally reduced based on the orientation of the normal of the fluidizing panel. This corresponded to a large z force reduction when the probe was moving in a vertical direction and the bottom chamber was fluidized (Fig. 4.4 blue region). In contrast, we see only a slight z force reduction when the probe is moving vertically and the side panel is fluidized (Fig. 4.4 blue region). When the probe was instead moving in the horizontal plane, a smaller vertical (z) force reduction was seen when the bottom panel was fluidized (Fig. 4.4 white region). When the side panel was fluidized and the probe was moving horizontally, we again see only fractional force reduction in the z direction (Fig. 4.4 white region).

Overall, we found that we only measure significant force reduction in an axis (z) if a fluidizing panel is pointed in that axes (bottom panel points in the z direction). Within this case, when the fluidizing surface was aligned with the direction of motion we saw a large force reduction, and even when the fluidizing surface was not aligned with the direction of motion we still see a (smaller) force reduction.

4.4.2 Horizontal Force Reduction

In the following section, we once again moved the robot arm with attached probe in a complex path through granular media, but this time examined the horizontal (y) forces over the same path for the following fluidization cases: 1) no fluidization, 2) side panel fluidization (34.5 kPa) where the fluidizing surface was pointed away from the direction of motion, 3) side panel fluidization (34.5 kPa) where the fluidizing surface was pointed orthogonal to the direction

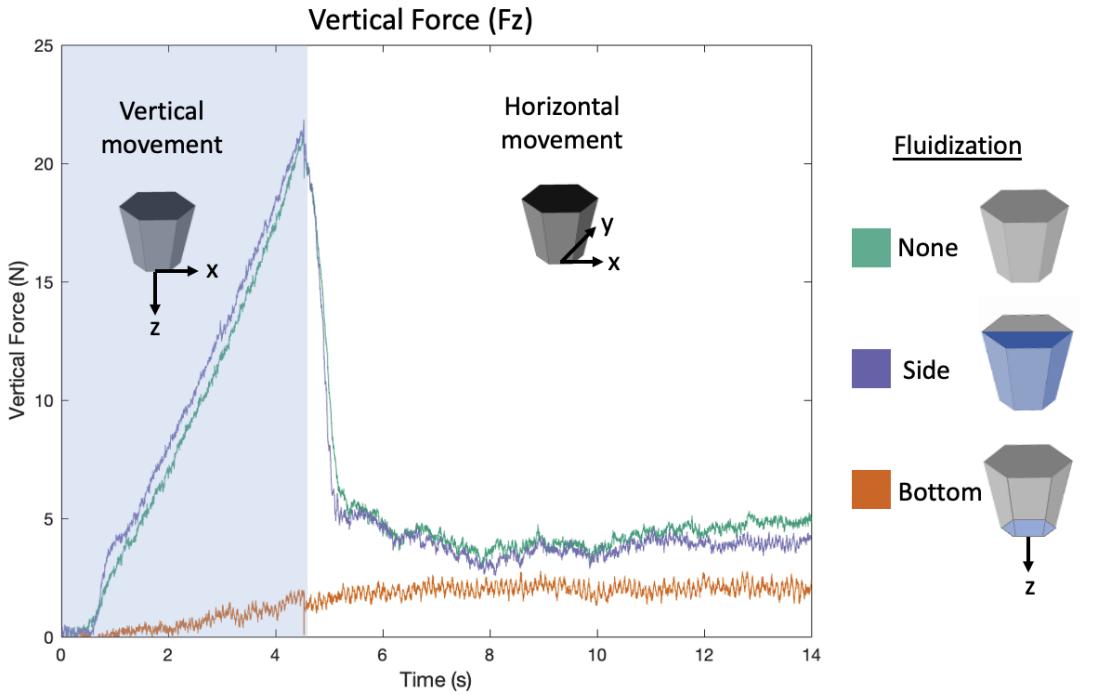

Figure 4.4: Vertical force over time for a fluidizing probe moved in a complex path through granular media showed that forces are reduced in the direction of fluidization and force reduction was highest when the direction of motion aligned with the normal to the fluidizing surface (blue region).

of motion, and 4) side panel fluidization (34.5 kPa) where the fluidizing surface was pointed towards the direction of motion (Fig. 4.5). We found that force reduction along the *y* axis due to fluidization only occurred when the direction of motion had a component in that axis (Fig. 4.5 blue region). Within this region, the magnitude of force reduction was greatest when the fluidizing surface was pointed in the direction of motion (orange). The next greatest reduction in drag force occurred when half the fluidizing surface pointed in the direction of motion (pink), and even when the fluidizing surface was pointed away from the direction of motion (purple), there was still some force reduction over the non-fluid case.

Our findings agreed with the trends found in the vertical force case: the largest force reduction was found when the fluidizing surface was aligned both with the direction of motion, and with the axis that we are examining. Surprisingly, we found that even when the fluidization direction was pointed opposite the direction of movement, the force in that plane was still reduced compared to the non-fluidizing case. One hypothesis for this could be that generating fluidization in any direction creates a path for the granular material to flow around the probe, reducing forces on the probe.

4.5 3D RFT with Fluidization Scaling Factor

In the following section we integrated the scaling factor from the vertical intrusion experiments (Fig. 4.1d) into 3D Resistive Force Theory (3D-RFT) [88, 94] in order to predict forces on an intruder with fluidizing surfaces. RFT is a method for predicting intrusion forces on bodies moving in granular media by segmenting a body into small elements and then determining the force on each element using empirical results dependent on the orientation of the element and the direction of movement [88], scaling with depth.

We added the pressure and depth dependent scaling factor as an additional multiplier on top of 3D RFT, and predicted the resistive forces on an intruder under the same fluidization cases

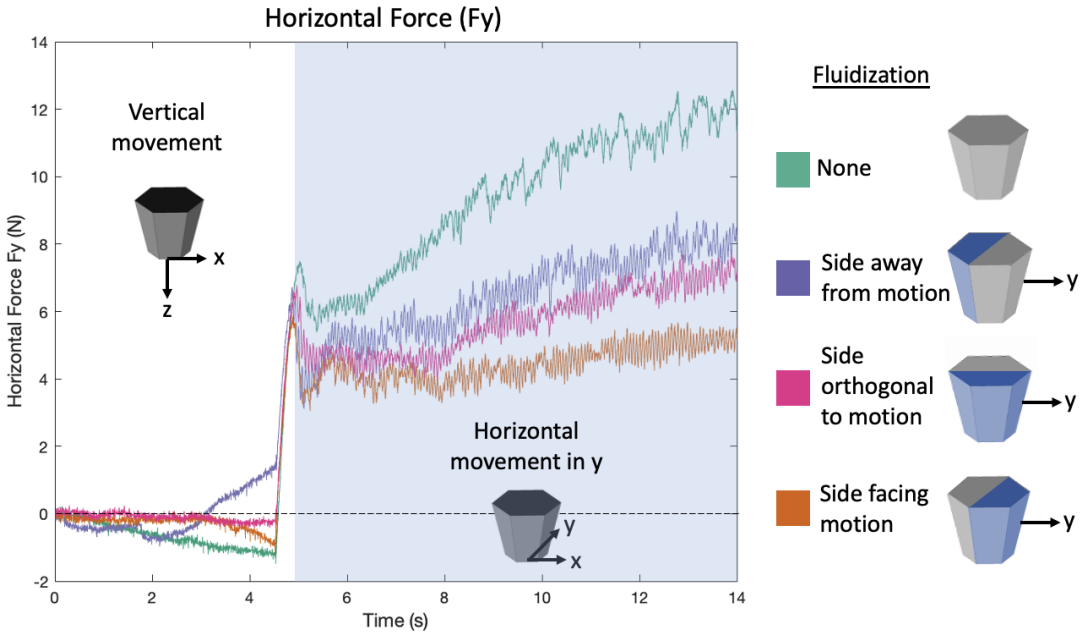

Figure 4.5: Horizontal force in the y direction over time for a fluidizing probe moved in a complex path through granular media showed that forces were reduced when the direction of movement aligned with the normal to the fluidizing surface (blue region).

and path used in the previous section (Fig. 4.3b).

We found good shape agreement between the predicted resistive forces in both the vertical (z) and horizontal (y) directions (Fig. 4.6a and Fig. 4.6b respectively), which can be contrasted to the experimental results found in Figure 4.4 and Figure 4.5 respectively. For vertical force, we found that RFT over predicted force across all cases under predicted the force reduction when the bottom panel was fluidized, but captured the correct nature of the plot over both vertical and horizontal movement. For the horizontal force, RFT both correctly captured the shape of the force curves, as well as the magnitude in the fluidizing cases. In the un-fluidized case, it again slightly over-predicted the force, this time while moving in the horizontal plane.

Surprisingly, RFT also captured the force reduction in the case where the fluidizing panel is pointed opposite the direction of motion. Overall, 3D RFT with our added fluidization factor offers an exciting avenue for the design of robots with fluidizing panels by providing a strategy for optimizing the shape and fluid surface placement along a robot body to reduce drag in desired

directions.

4.6 Robot Demonstration

In the following section we demonstrated a digging robot using two fluidizing probes with a linear actuator body (Fig. 4.7a). The robot head and tail sections were each composed of a fluidizing probe with two internal chambers and externally connected pneumatic lines. The midsection of the robot was composed of a linear actuator wrapped in a sleeve to prevent sand particles from jamming the actuator. The whole system was controlled by a volumetric control board (Fig. 4.7b). The control board consisted of an Arduino Mega, relays and valves for switching the pneumatic lines on and off, a connection to house air, and a connection to power for the linear actuator.

A full actuation cycle for the two segment robot consisted of the following sequence: 1) the front chamber was fully fluidized and the back chamber was un-fluidized and anchored, 2) the linear actuator extended, pushing the fluidizing front chamber forwards, 3) the front chamber was depressurized to serve as an anchor point and the back chamber was fluidized, and 4) the linear actuator retracted, pulling the fluidized back chamber forwards (Fig. 4.8a).

The robot was then submerged into a bed filled with granular material (0.3 mm glass spheres) and actuated at a speed of six seconds per cycle (three seconds to extend, three seconds to retract). Video tracking was done using small colored rods attached to the head and tail segments that protruded out of the sand.

4.6.1 Robot Performance

We found that, when cyclically actuated, the robot moved at a speed of .34 cm/s, or 2.0 cm/cycle (Fig. 4.8b orange trace). With no fluidization and only linear actuator movement, the resulting speed of the robot was 0 cm/s and the body segments did not move appreciably (Fig.

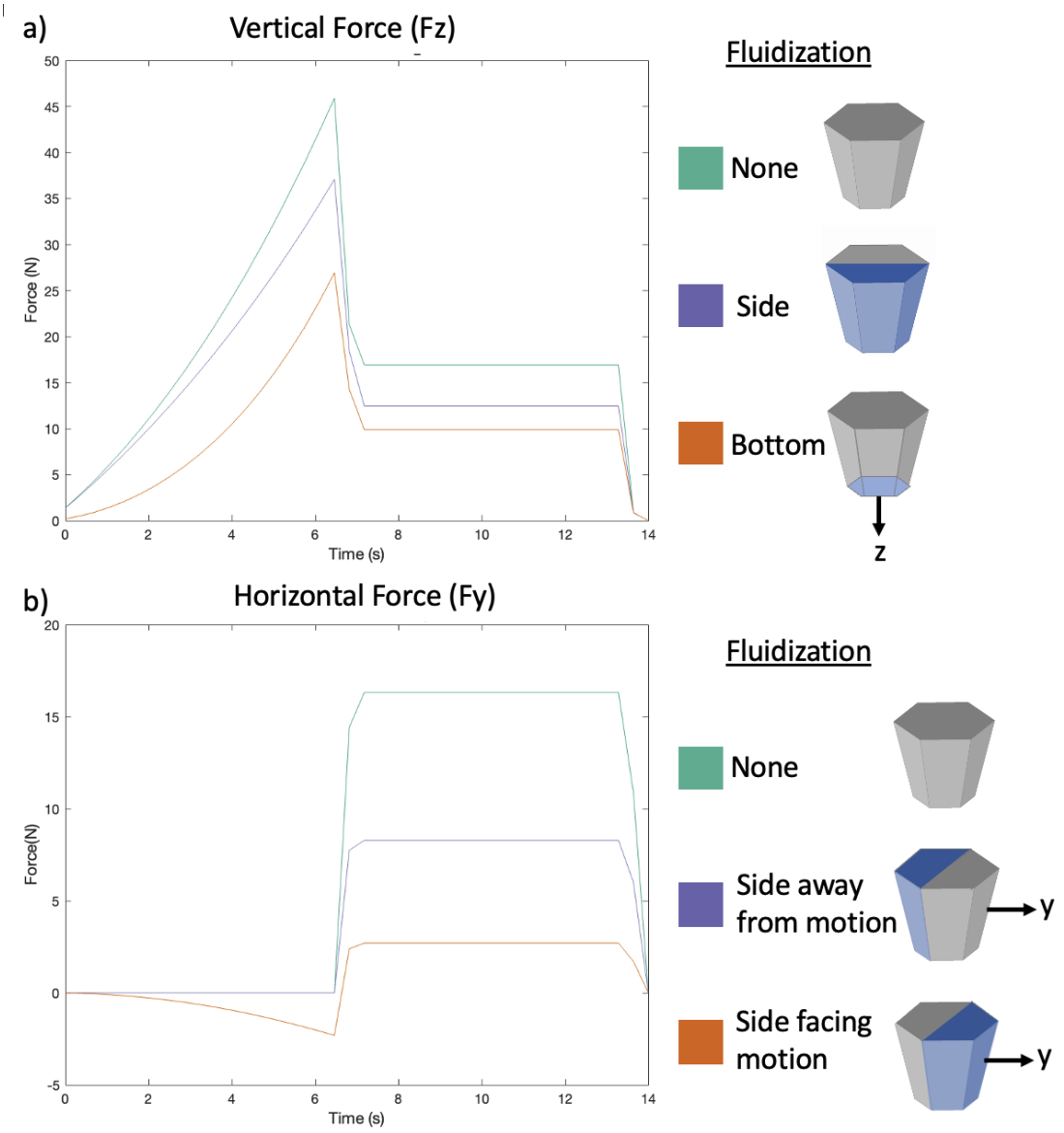

Figure 4.6: 3D RFT with a pressure-depth dependent scaling factor predicted the nature of intrusion forces over a complex path. a) Vertical force predicted by fluidizing 3D RFT over the same path and with the same fluidization cases seen in Figure 4.4. b) Horizontal force predicted by fluidizing 3D RFT over over the same path and with the same fluidization cases seen in Figure 4.5.

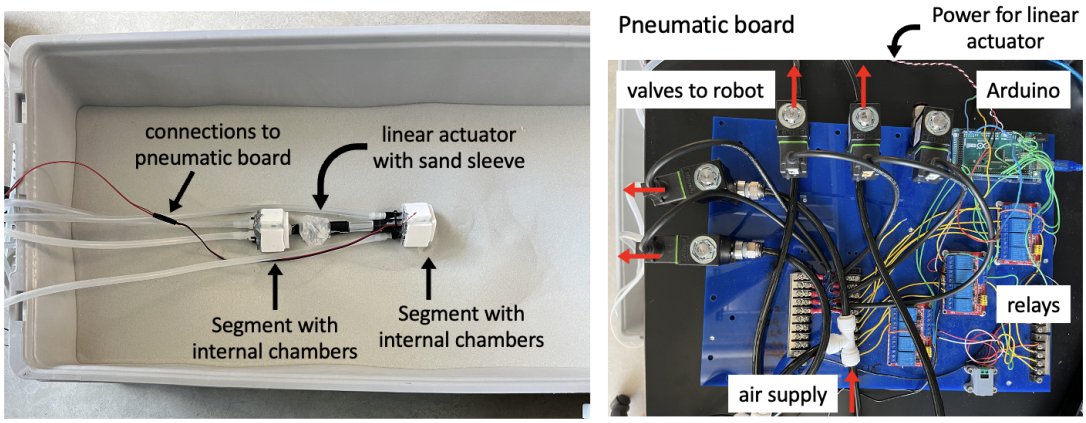

Figure 4.7: Robot design. a) Robot head and tail sections were composed of fluidizing probes, each with two internal chambers and externally connected pneumatic lines. The midsection of the robot was composed of a linear actuator wrapped in a sleeve to stop sand particles from jamming the actuator. b) Volumetric control board for actuating robot. Control board consisted of an Arduino Mega, relays and valves for switching the pneumatic lines on and off, a connection to house air, and a power connection for the linear actuator.

4.8b blue trace). When both segments were always fluidized, the linear actuator movement created movement in the tail segment only (Fig. 4.8b green trace), and the resulting speed was 0 cm/s.

Of these three movement strategies, only the anchor-extend strategy using cyclical fluidization produced forward movement. This is similar to the anchoring-fluidization strategy seen in the Venus clam [84]. In the no fluidization case, even though the linear actuator was cycling, neither segments showed large movement in the granular media. We hypothesized that the stall torque of the linear actuator was less than the large subterranean forces that exist in the granular media, resulting in very little actuator movement. In the constant fluidization case, forces were reduced such that the linear actuator movement was visible (Fig. 4.8b green trace), but the robot still did not make forward progress. Instead, front of the robot remained anchored while the rear gradually un-anchored itself. Over the course of about a minute, the rear of the robot gradually rose to the surface of the tank.

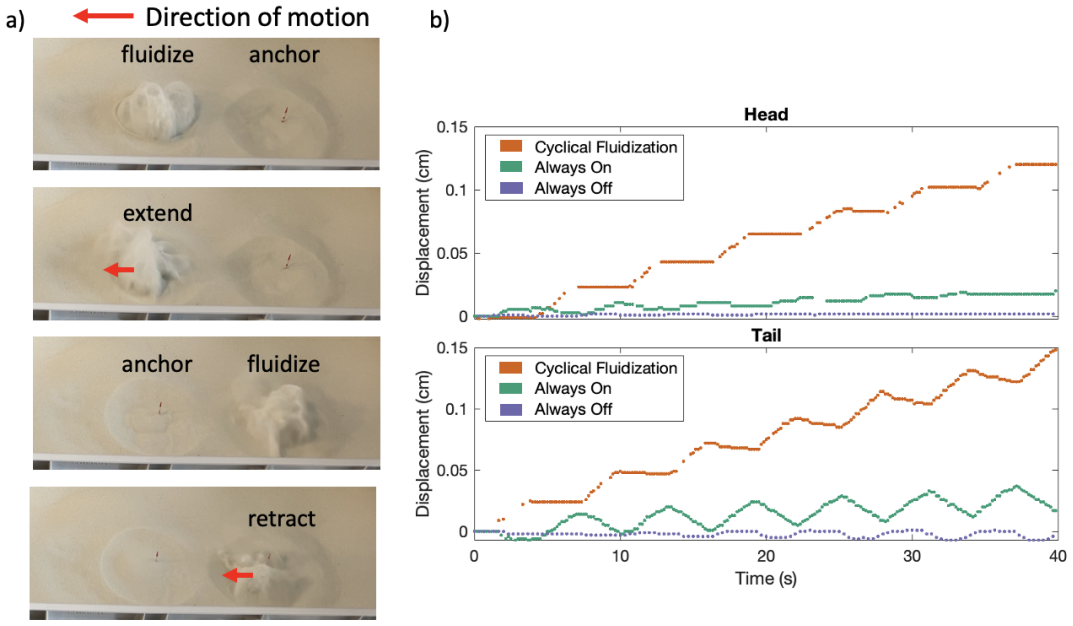

Figure 4.8: Subterranean locomotion. a) An actuation cycle consisted of the following sequence: Front chamber was fluidized and the linear actuator extended the front forwards while the back chamber was anchored and not fluidized. Front fluidization was turned off and front became an anchor. Back chamber was fluidized and linear actuator was retracted. Back chamber fluidization was then turned off, and the cycle repeated. Each actuation cycle lasted six seconds. b) Robot motion over time for head and tail sections. Forwards motion was only seen in the cyclical actuation scenario: for both the scenario where fluidization was kept on always and the scenario where no fluidization was used, the robot did not make forward progress, and the tail ended up surfacing.

4.7 Discussion

Fluidizing robot body surfaces can enable fast and energy-efficient subterranean locomotion by modifying drag along the robot body to reduce forces in movement directions. In the future, using our fluidizing scaling factor coupled with RFT can enable the intelligent design of robot body shapes and placement of fluidizing surfaces along the robot body in order to elicit certain drag properties, thus enabling the optimization of digging robot designs. Fluidization offers a promising future direction for enhancing the speed of soft-bodied digging robots, which are ideal for use in subterranean locomotion because components are less likely than their rigid counterparts to get jammed up with granular material. The flip side of soft components is that they cannot exert large forces on their environment, an issue which can be resolved by the use of fluidizing surfaces. As an added benefit for pneumatically-driven soft robots, the addition to fluidizing panels does not complicate the actuation scheme.

Chapter 4, or portion thereof, is being prepared for publication of the material. Lathrop, Emily; Jadhav, Saurabh; Tolley, Michael T.; Gravish, Nick. The dissertation author was the primary investigator and author of this paper.

Chapter 5

Summary

In this dissertation, I examined robot-environment interactions in three scenarios: over loose rock, in confined spaces, and underground in granular media. In each project, I explored how robot body morphology can be modified to reduce failure and improve performance in a specific natural terrain scenario. In all three projects, I first examined failure cases at the interface between a robot body and the terrain in which it inhabits. I then used mechanisms to modify either stiffness or drag directionally to improve physical interactions between each robot and its environment. In the second and third chapters, I modified compliance at the level of a robot foot and leg respectively. In the fourth chapter, instead of modifying compliance I focused on altering drag forces by modifying the properties of the surrounding terrain. This focus on material properties and mechanical design can enable more robust robot design without increasing sensing and control requirements when moving over complex natural terrain.

In Chapter 2, I developed robot feet that could conform around uneven terrain and stiffen, allowing a robot to maintain reliable contact surfaces even in the presence of loose, rocky, or otherwise irregular ground. I reduced shear failure at the connection point between the rigid robot leg and soft robot foot, increasing the usability of granular jamming actuators for load-

bearing applications. The variable stiffness properties of these feet allowed them to conform to irregular terrain yet also transmit forces effectively. A key metric used to evaluate these new foot designs was measuring the area of contact surfaces around a step-shaped obstacle. We focused on increasing the area in contact with the ground by adding internal structures. In the future, it would be interesting to also examine the effect that changing foot diameter has on performance. We hypothesize that some portion of the increased performance between the rigid foot and the granular foot was likely due to the increased diameter of the foot itself, regardless of variable stiffness properties. It would be interesting to explore if robots with larger feet would exhibit performance benefits on natural terrain. Intuitively, we might expect a larger diameter foot to spread the weight of a robot over a larger area, allowing for more contact points and reducing pressure. This offers a promising strategy for designing robots to move over terrain that can shift underfoot when heavily loaded (rock piles, sand dunes, other granular media).

In Chapter 3, we zoom out from robot feet to examine compliance higher up on the chain, at the scale of a robot leg. In Chapter 3, I created directionally compliant robot legs that were stiff in load-bearing directions for locomotion yet could passively compress to allow a robot to fit into confined spaces. These appendages were successful at moving through low friction walls, making them ideal for environments such as pipes and ducting, but sometimes failed when interacting with walls featuring rough protrusions or walls with high friction coefficients. Specifically, we observed that when the friction coefficient of the ground was lower than that of the walls, the robot could lose traction and the legs could jam themselves between the walls, stopping forward progress. One possible solution could be to alter the frictional properties of the outside of the legs to create low friction surfaces on the parts of the leg that encounter walls, and high friction surfaces on the parts of the leg that generate traction. On the flip side, this behavior is very similar to a move used in rock climbing called stemming, suggesting that it may be possible to create climbing behaviors with these appendages by adjusting relative friction.

In Chapter 4, we again zoom out, this time to the scale of a robot body. In this chapter, I

explored strategies for subterranean locomotion that harness the properties of granular media and use granular fluidization to reduce drag directionally on across robot body surfaces. In Chapter 2 I altered the properties of granular media inside a robot foot, here we again altered the properties of granular media, but this time in the environment. Instead of using vacuum to decrease the air surrounding granular media and solidify it, we increased airflow around granular media, creating liquid-like properties. This approach offers a promising avenue for enhancing robot locomotion in granular media, although there are still open questions about the suitability of using resistive force theory (RFT) to model a fluidized granular material, since there may be flow effects that cannot be captured by RFT but have significant force and drag effects. For example, RFT was not able to predict the force reduction observed when a fluidizing surface was oriented away from the direction of motion of a moving object (Fig. 4.5). In the future, it could be interesting to examine if discrete element methods can better predict forces on fluidized granular intruders.

Overall, natural environments feature complex, hard to model interactions: loose rock moves about underfoot when stepped on, walls and tunnels in nature have geometry that varies spatially, and granular materials exhibit non-Newtonian properties. Natural terrain also features tough-to-measure properties with large parameter variations. Taking rocky ground as an example, parameters such as rock size, shape, friction, and material composition can vary greatly, and are hard to generalize. A unifying goal between all of these projects was to create versatile robots that were robust to parameter variations in natural terrains. The granular jamming feet provided performance benefits over multiple sizes and shapes of rocks, the telescoping legs were adaptable to multiple widths of tunnels, and granular fluidization can be used on granular media of many particle sizes and densities.

This dissertation is a step towards enabling new robot capabilities and expanding the range of environments that robots can successfully navigate, allowing robots to replace humans in dangerous, difficult, or hard to access environments. In the future, the morphology modifications proposed in this dissertation could be modularly applied to the feet, legs, or body panels of

existing industrial robots to improve their performance in target environments.

Bibliography

[1] H. Kimura, Y. Fukuoka, and A. H. Cohen, "Adaptive dynamic walking of a quadruped robot on natural ground based on biological concepts," *The International Journal of Robotics Research*, vol. 26, no. 5, pp. 475–490, 2007.

[2] M. Eich, F. Grimminger, S. Bosse, D. Spenneberg, and F. Kirchner, "Asguard: A hybrid-wheel security and sar-robot using bio-inspired locomotion for rough terrain," *Proceedings ROBIO*, vol. 20082008, pp. 774–779, 2008.

[3] M. Hutter, C. Gehring, D. Jud, A. Lauber, C. D. Bellicoso, V. Tsounis, J. Hwangbo, K. Bodie, P. Fankhauser, M. Bloesch, *et al.*, "Anymal-a highly mobile and dynamic quadrupedal robot," in *2016 IEEE/RSJ international conference on intelligent robots and systems (IROS)*, pp. 38–44, IEEE, 2016.

[4] J. Lee, J. Hwangbo, L. Wellhausen, V. Koltun, and M. Hutter, "Learning quadrupedal locomotion over challenging terrain," *Science robotics*, vol. 5, no. 47, p. eabc5986, 2020.

[5] U. Saranli, M. Buehler, and D. E. Koditschek, "Rhex: A simple and highly mobile hexapod robot," *The International Journal of Robotics Research*, vol. 20, no. 7, pp. 616–631, 2001.

[6] J. A. Cobano, J. Estremera, and P. Gonzalez de Santos, "Accurate tracking of legged robots on natural terrain," *Autonomous Robots*, vol. 28, no. 2, pp. 231–244, 2010.

[7] D. Goldschmidt, F. Wörgötter, and P. Manoonpong, "Biologically-inspired adaptive obstacle negotiation behavior of hexapod robots," *Frontiers in neurorobotics*, vol. 8, p. 3, 2014.

[8] D. Belter, P. Łabecki, and P. Skrzypczyński, "Adaptive motion planning for autonomous rough terrain traversal with a walking robot," *Journal of Field Robotics*, vol. 33, no. 3, pp. 337–370, 2016.

[9] J. Faigl and P. Čížek, "Adaptive locomotion control of hexapod walking robot for traversing rough terrains with position feedback only," *Robotics and Autonomous Systems*, vol. 116, pp. 136–147, 2019.

[10] H. Date, Y. Hoshi, M. Sampei, and S. Nakaura, "Locomotion control of a snake robot with constraint force attenuation," in *Proceedings of the 2001 American Control Conference.(Cat. No. 01CH37148)*, vol. 1, pp. 113–118, IEEE, 2001.

[11] P. Liljeback, K. Y. Pettersen, Ø. Stavdahl, and J. T. Gravdahl, "Snake robot locomotion in environments with obstacles," *IEEE/ASME Transactions on Mechatronics*, vol. 17, no. 6, pp. 1158–1169, 2011.

[12] H. Marvi, C. Gong, N. Gravish, H. Astley, M. Travers, R. L. Hatton, J. R. Mendelson III, H. Choset, D. L. Hu, and D. I. Goldman, "Sidewinding with minimal slip: Snake and robot ascent of sandy slopes," *Science*, vol. 346, no. 6206, pp. 224–229, 2014.

[13] Q. Fu, H. C. Astley, and C. Li, "Snakes combine vertical and lateral bending to traverse uneven terrain," *Bioinspiration & Biomimetics*, vol. 17, no. 3, p. 036009, 2022.

[14] K. J. Huang, S.-C. Chen, Y. C. Chou, S.-Y. Shen, C.-H. Li, and P.-C. Lin, "Experimental validation of a leg-wheel hybrid mobile robot quattroped," in *2011 IEEE International Conference on Robotics and Automation*, pp. 2976–2977, IEEE, 2011.

[15] L. Bruzzone and P. Fanghella, "Mantis: hybrid leg-wheel ground mobile robot," *Industrial Robot: An International Journal*, vol. 41, no. 1, pp. 26–36, 2014.

[16] Y.-S. Kim, G.-P. Jung, H. Kim, K.-J. Cho, and C.-N. Chu, "Wheel transformer: A wheel-leg hybrid robot with passive transformable wheels," *IEEE Transactions on Robotics*, vol. 30, no. 6, pp. 1487–1498, 2014.

[17] D.-Y. Lee, S.-R. Kim, J.-S. Kim, J.-J. Park, and K.-J. Cho, "Origami wheel transformer: A variable-diameter wheel drive robot using an origami structure," *Soft robotics*, vol. 4, no. 2, pp. 163–180, 2017.

[18] D. Drotman, S. Jadhav, M. Karimi, P. Dezonia, and M. T. Tolley, "3d printed soft actuators for a legged robot capable of navigating unstructured terrain," in *2017 IEEE International Conference on Robotics and Automation (ICRA)*, pp. 5532–5538, IEEE, 2017.

[19] J. Kacprzyk and W. Pedrycz, *Springer handbook of computational intelligence*. Springer, 2015.

[20] A. Cangelosi, J. Bongard, M. H. Fischer, and S. Nolfi, "Embodied intelligence," in *Springer Handbook of Computational Intelligence*, pp. 697–714, Springer, 2015.

[21] M. Calisti, G. Picardi, and C. Laschi, "Fundamentals of soft robot locomotion," *Journal of The Royal Society Interface*, vol. 14, no. 130, p. 20170101, 2017.

[22] F. Iida and C. Laschi, "Soft robotics: Challenges and perspectives," *Procedia Computer Science*, vol. 7, pp. 99–102, 2011.

[23] S. Kim, C. Laschi, and B. Trimmer, "Soft robotics: a bioinspired evolution in robotics," *Trends in biotechnology*, vol. 31, no. 5, pp. 287–294, 2013.

[24] M. T. Northen, C. Greiner, E. Arzt, and K. L. Turner, "A gecko-inspired reversible adhesive," *Advanced Materials*, vol. 20, no. 20, pp. 3905–3909, 2008.

[25] A. G. Gillies, J. Kwak, and R. S. Fearing, "Controllable particle adhesion with a magnetically actuated synthetic gecko adhesive," *Advanced Functional Materials*, vol. 23, no. 26, pp. 3256–3261, 2013.

[26] K. A. Daltorio, A. D. Horchler, S. Gorb, R. E. Ritzmann, and R. D. Quinn, "A small wall-walking robot with compliant, adhesive feet," in *2005 IEEE/RSJ International Conference on Intelligent Robots and Systems*, pp. 3648–3653, IEEE, 2005.

[27] A. Spröwitz, A. Tuleu, M. Vespignani, M. Ajallooeian, E. Badri, and A. J. Ijspeert, "Towards dynamic trot gait locomotion: Design, control, and experiments with cheetah-cub, a compliant quadruped robot," *The International Journal of Robotics Research*, vol. 32, no. 8, pp. 932–950, 2013.

[28] E. Brown, N. Rodenberg, J. Amend, A. Mozeika, E. Steltz, M. R. Zakin, H. Lipson, and H. M. Jaeger, "Universal robotic gripper based on the jamming of granular material," *Proceedings of the National Academy of Sciences*, vol. 107, no. 44, pp. 18809–18814, 2010.

[29] A. Hosoi and D. I. Goldman, "Beneath our feet: strategies for locomotion in granular media," *Annu. Rev. Fluid Mech*, vol. 47, no. 1, pp. 431–453, 2015.

[30] S. Kim, P. M. Wensing, *et al.*, "Design of dynamic legged robots," *Foundations and Trends® in Robotics*, vol. 5, no. 2, pp. 117–190, 2017.

[31] S. Hauser, P. Eckert, A. Tuleu, and A. Ijspeert, "Friction and damping of a compliant foot based on granular jamming for legged robots," in *2016 6th IEEE International Conference on Biomedical Robotics and Biomechatronics (BioRob)*, pp. 1160–1165, Ieee, 2016.

[32] D. H. Gray and H. Ohashi, "Mechanics of fiber reinforcement in sand," *Journal of geotechnical engineering*, vol. 109, no. 3, pp. 335–353, 1983.

[33] T. Majmudar, M. Sperl, S. Luding, and R. P. Behringer, "Jamming transition in granular systems," *Physical review letters*, vol. 98, no. 5, p. 058001, 2007.

[34] H. M. Jaeger, "Celebrating soft matter's 10th anniversary: Toward jamming by design," *Soft matter*, vol. 11, no. 1, pp. 12–27, 2015.

[35] E. Brown, N. Rodenberg, J. Amend, A. Mozeika, E. Steltz, M. R. Zakin, H. Lipson, and H. M. Jaeger, "Universal robotic gripper based on the jamming of granular material," *Proceedings of the National Academy of Sciences*, vol. 107, no. 44, pp. 18809–18814, 2010.

[36] J. R. Amend, E. Brown, N. Rodenberg, H. M. Jaeger, and H. Lipson, "A positive pressure universal gripper based on the jamming of granular material," *IEEE Transactions on Robotics*, vol. 28, no. 2, pp. 341–350, 2012.

[37] E. Steltz, A. Mozeika, N. Rodenberg, E. Brown, and H. M. Jaeger, "Jsel: Jamming skin enabled locomotion," in *2009 IEEE/RSJ International Conference on Intelligent Robots and Systems*, pp. 5672–5677, IEEE, 2009.

[38] T. Mitsuda, S. Kuge, M. Wakabayashi, and S. Kawamura, "Wearable haptic display by the use of a particle mechanical constraint," in *Proceedings 10th Symposium on Haptic Interfaces for Virtual Environment and Teleoperator Systems. HAPTICS 2002*, pp. 153–158, IEEE, 2002.

[39] T. Ranzani, G. Gerboni, M. Cianchetti, and A. Menciassi, "A bioinspired soft manipulator for minimally invasive surgery," *Bioinspiration & biomimetics*, vol. 10, no. 3, p. 035008, 2015.

[40] C. Li, P. B. Umbanhowar, H. Komsuoglu, D. E. Koditschek, and D. I. Goldman, "Sensitive dependence of the motion of a legged robot on granular media," *Proceedings of the National Academy of Sciences*, vol. 106, no. 9, pp. 3029–3034, 2009.

[41] A. Rafsanjani, Y. Zhang, B. Liu, S. M. Rubinstein, and K. Bertoldi, "Kirigami skins make a simple soft actuator crawl," *Science Robotics*, vol. 3, no. 15, p. eaar7555, 2018.

[42] I. R. Manchester, U. Mettin, F. Iida, and R. Tedrake, "Stable dynamic walking over uneven terrain," *The International Journal of Robotics Research*, vol. 30, no. 3, pp. 265–279, 2011.

[43] M. Bjelonic, N. Kottege, and P. Beckerle, "Proprioceptive control of an over-actuated hexapod robot in unstructured terrain," in *2016 IEEE/RSJ International Conference on Intelligent Robots and Systems (IROS)*, pp. 2042–2049, IEEE, 2016.

[44] A. Najmuddin, Y. Fukuoka, and S. Ochiai, "Experimental development of stiffness adjustable foot sole for use by bipedal robots walking on uneven terrain," in *2012 IEEE/SICE International Symposium on System Integration (SII)*, pp. 248–253, IEEE, 2012.

[45] R. P. Behringer and B. Chakraborty, "The physics of jamming for granular materials: a review," *Reports on Progress in Physics*, vol. 82, no. 1, p. 012601, 2018.

[46] B. Reubens, J. Poesen, F. Danjon, G. Geudens, and B. Muys, "The role of fine and coarse roots in shallow slope stability and soil erosion control with a focus on root system architecture: a review," *Trees*, vol. 21, no. 4, pp. 385–402, 2007.

[47] H. G. Poulos, "Design of reinforcing piles to increase slope stability," *Canadian Geotechnical Journal*, vol. 32, no. 5, pp. 808–818, 1995.

[48] D. P. Holland, E. J. Park, P. Polygerinos, G. J. Bennett, and C. J. Walsh, "The soft robotics toolkit: Shared resources for research and design," *Soft Robotics*, vol. 1, no. 3, pp. 224–230, 2014.

[49] C. Creager, V. Asnani, H. Oravec, and A. Woodward, "Drawbar pull (dp) procedures for off-road vehicle testing," 2017.

[50] M. Kalakrishnan, J. Buchli, P. Pastor, M. Mistry, and S. Schaal, "Fast, robust quadruped locomotion over challenging terrain," in *2010 IEEE International Conference on Robotics and Automation*, pp. 2665–2670, IEEE, 2010.

[51] M. Bjelonic, N. Kottege, T. Homberger, P. Borges, P. Beckerle, and M. Chli, "Weaver: Hexapod robot for autonomous navigation on unstructured terrain," *Journal of Field Robotics*, vol. 35, no. 7, pp. 1063–1079, 2018.

[52] A. Bouman, M. F. Ginting, N. Alatur, M. Palieri, D. D. Fan, T. Touma, T. Pailevanian, S.-K. Kim, K. Otsu, J. Burdick, *et al.*, "Autonomous spot: Long-range autonomous exploration of extreme environments with legged locomotion," in *2020 IEEE/RSJ International Conference on Intelligent Robots and Systems (IROS)*, pp. 2518–2525, IEEE, 2020.

[53] T. Wang, J. Whitman, M. Travers, and H. Choset, "Directional compliance in obstacle-aided navigation for snake robots," in *2020 American Control Conference (ACC)*, pp. 2458–2463, IEEE, 2020.

[54] H. C. Astley, J. M. Rieser, A. Kaba, V. M. Paez, I. Tomkinson, J. R. Mendelson, and D. I. Goldman, "Side-impact collision: mechanics of obstacle negotiation in sidewinding snakes," *Bioinspiration & Biomimetics*, vol. 15, no. 6, p. 065005, 2020.

[55] H. Chang, J. Chang, G. Clifton, and N. Gravish, "Anisotropic compliance of robot legs improves recovery from swing-phase collisions," *Bioinspiration & Biomimetics*, 2021.

[56] K. Jayaram and R. J. Full, "Cockroaches traverse crevices, crawl rapidly in confined spaces, and inspire a soft, legged robot," *Proceedings of the National Academy of Sciences*, vol. 113, no. 8, pp. E950–E957, 2016.

[57] N. S. Roslin, A. Anuar, M. F. A. Jalal, and K. S. M. Sahari, "A review: Hybrid locomotion of in-pipe inspection robot," *Procedia Engineering*, vol. 41, pp. 1456–1462, 2012.

[58] L. Bruzzone and G. Quaglia, "Locomotion systems for ground mobile robots in unstructured environments," *Mechanical sciences*, vol. 3, no. 2, pp. 49–62, 2012.

[59] S. W. Gart and C. Li, "Body-terrain interaction affects large bump traversal of insects and legged robots," *Bioinspiration & biomimetics*, vol. 13, no. 2, p. 026005, 2018.

[60] N. Gravish, D. Monaenkova, M. A. Goodisman, and D. I. Goldman, "Climbing, falling, and jamming during ant locomotion in confined environments," *Proceedings of the National Academy of Sciences*, vol. 110, no. 24, pp. 9746–9751, 2013.

[61] R. D. Maladen, Y. Ding, C. Li, and D. I. Goldman, "Undulatory swimming in sand: subsurface locomotion of the sandfish lizard," *science*, vol. 325, no. 5938, pp. 314–318, 2009.

[62] C. Laschi, M. Cianchetti, B. Mazzolai, L. Margheri, M. Follador, and P. Dario, "Soft robot arm inspired by the octopus," *Advanced robotics*, vol. 26, no. 7, pp. 709–727, 2012.

[63] Y. Ozkan-Aydin and D. I. Goldman, "Self-reconfigurable multilegged robot swarms collectively accomplish challenging terradynamic tasks," *Science Robotics*, vol. 6, no. 56, p. eabf1628, 2021.

[64] P. Hebert, M. Bajracharya, J. Ma, N. Hudson, A. Aydemir, J. Reid, C. Bergh, J. Borders, M. Frost, M. Hagman, *et al.*, "Mobile manipulation and mobility as manipulation—design and algorithms of robosimian," *Journal of Field Robotics*, vol. 32, no. 2, pp. 255–274, 2015.

[65] G. Bledt, M. J. Powell, B. Katz, J. Di Carlo, P. M. Wensing, and S. Kim, "Mit cheetah 3: Design and control of a robust, dynamic quadruped robot," in *2018 IEEE/RSJ International Conference on Intelligent Robots and Systems (IROS)*, pp. 2245–2252, IEEE, 2018.

[66] C. Semini, N. G. Tsagarakis, E. Guglielmino, M. Focchi, F. Cannella, and D. G. Caldwell, "Design of hyq–a hydraulically and electrically actuated quadruped robot," *Proceedings of the Institution of Mechanical Engineers, Part I: Journal of Systems and Control Engineering*, vol. 225, no. 6, pp. 831–849, 2011.

[67] R. Buchanan, T. Bandyopadhyay, M. Bjelonic, L. Wellhausen, M. Hutter, and N. Kottege, "Walking posture adaptation for legged robot navigation in confined spaces," *IEEE Robotics and Automation Letters*, vol. 4, no. 2, pp. 2148–2155, 2019.

[68] P. Birkmeyer, K. Peterson, and R. S. Fearing, "Dash: A dynamic 16g hexapedal robot," in *2009 IEEE/RSJ international conference on intelligent robots and systems*, pp. 2683–2689, IEEE, 2009.

[69] D. W. Haldane, K. C. Peterson, F. L. G. Bermudez, and R. S. Fearing, "Animal-inspired design and aerodynamic stabilization of a hexapedal millirobot," in *2013 IEEE International Conference on Robotics and Automation*, pp. 3279–3286, IEEE, 2013.

[70] Y.-S. Kim, G.-P. Jung, H. Kim, K.-J. Cho, and C.-N. Chu, "Wheel transformer: A miniaturized terrain adaptive robot with passively transformed wheels," in *2013 IEEE International Conference on Robotics and Automation*, pp. 5625–5630, IEEE, 2013.

[71] B. W. Satzinger, C. Lau, M. Byl, and K. Byl, "Experimental results for dexterous quadruped locomotion planning with robosimian," in *Experimental Robotics*, pp. 33–46, Springer, 2016.

[72] P. E. Dupont, J. Lock, B. Itkowitz, and E. Butler, "Design and control of concentric-tube robots," *IEEE Transactions on Robotics*, vol. 26, no. 2, pp. 209–225, 2009.

[73] T. K. Morimoto and A. M. Okamura, "Design of 3-d printed concentric tube robots," *IEEE Transactions on Robotics*, vol. 32, no. 6, pp. 1419–1430, 2016.

[74] C. Yu, K. Crane, and S. Coros, "Computational design of telescoping structures," *ACM Transactions on Graphics (TOG)*, vol. 36, no. 4, pp. 1–9, 2017.

[75] J. Hodgins, "Legged robots on rough terrain: experiments in adjusting step length," in *Proceedings. 1988 IEEE International Conference on Robotics and Automation*, pp. 824–826, IEEE, 1988.

[76] A. Nubiola, M. Slamani, and I. A. Bonev, "A new method for measuring a large set of poses with a single telescoping ballbar," *Precision Engineering*, vol. 37, no. 2, pp. 451–460, 2013.

[77] A. M. Hoover, S. Burden, X.-Y. Fu, S. S. Sastry, and R. S. Fearing, "Bio-inspired design and dynamic maneuverability of a minimally actuated six-legged robot," in *2010 3rd IEEE RAS & EMBS International Conference on Biomedical Robotics and Biomechatronics*, pp. 869–876, IEEE, 2010.

[78] C. Semini, V. Barasuol, T. Boaventura, M. Frigerio, M. Focchi, D. G. Caldwell, and J. Buchli, "Towards versatile legged robots through active impedance control," *The International Journal of Robotics Research*, vol. 34, no. 7, pp. 1003–1020, 2015.

[79] D. Rus and M. T. Tolley, "Design, fabrication and control of soft robots," *Nature*, vol. 521, no. 7553, pp. 467–475, 2015.

[80] C. Laughton, *Evaluation and prediction of tunnel boring machine performance in variable rock masses*. The University of Texas at Austin, 1998.

[81] D. Yalden, "The anatomy of mole locomotion," *Journal of Zoology*, vol. 149, no. 1, pp. 55–64, 1966.

[82] K. J. Quillin, "Kinematic scaling of locomotion by hydrostatic animals: ontogeny of peristaltic crawling by the earthworm lumbricus terrestris," *Journal of Experimental Biology*, vol. 202, no. 6, pp. 661–674, 1999.

[83] J. Che and K. M. Dorgan, "It's tough to be small: dependence of burrowing kinematics on body size," *Journal of Experimental Biology*, vol. 213, no. 8, pp. 1241–1250, 2010.

[84] H. Wei, Y. Zhang, T. Zhang, Y. Guan, K. Xu, X. Ding, and Y. Pang, "Review on bioinspired planetary regolith-burrowing robots," *Space Science Reviews*, vol. 217, no. 8, pp. 1–39, 2021.

[85] N. I. Kömle, P. Weiss, and K. L. Yung, "Considerations on a suction drill for lunar surface drilling and sampling: I. feasibility study," *Acta Geotechnica*, vol. 3, no. 3, pp. 201–214, 2008.

[86] K. Zacny, D. Currie, G. Paulsen, T. Szwarc, and P. Chu, "Development and testing of the pneumatic lunar drill for the emplacement of the corner cube reflector on the moon," *Planetary and Space Science*, vol. 71, no. 1, pp. 131–141, 2012.

[87] E. Montellà, M. Toraldo, B. Chareyre, and L. Sibille, "Localized fluidization in granular materials: Theoretical and numerical study," *Physical Review E*, vol. 94, no. 5, p. 052905, 2016.

[88] C. Li, T. Zhang, and D. I. Goldman, "A terradynamics of legged locomotion on granular media," *science*, vol. 339, no. 6126, pp. 1408–1412, 2013.

[89] P. Philippe and M. Badiane, "Localized fluidization in a granular medium," *Physical Review E*, vol. 87, no. 4, p. 042206, 2013.

[90] K. M. Dorgan, "The biomechanics of burrowing and boring," *Journal of Experimental Biology*, vol. 218, no. 2, pp. 176–183, 2015.

[91] D. P. Germann and J. P. Carbajal, "Burrowing behaviour of robotic bivalves with synthetic morphologies," *Bioinspiration & biomimetics*, vol. 8, no. 4, p. 046009, 2013.

[92] A. Winter, R. Deits, D. Dorsch, A. Slocum, A. Hosoi, *et al.*, "Razor clam to roboclam: burrowing drag reduction mechanisms and their robotic adaptation," *Bioinspiration & biomimetics*, vol. 9, no. 3, p. 036009, 2014.

[93] N. D. Naclerio, A. Karsai, M. Murray-Cooper, Y. Ozkan-Aydin, E. Aydin, D. I. Goldman, and E. W. Hawkes, "Controlling subterranean forces enables a fast, steerable, burrowing soft robot," *Science Robotics*, vol. 6, no. 55, p. eabe2922, 2021.

[94] L. K. Treers, C. Cao, and H. S. Stuart, "Granular resistive force theory implementation for three-dimensional trajectories," *IEEE Robotics and Automation Letters*, vol. 6, no. 2, pp. 1887–1894, 2021.

[95] C.-P. Liu, S. Bai, and L. Wang, "Resistance forces on an intruder penetrating partially fluidized granular media," *Physical Review E*, vol. 99, no. 1, p. 012903, 2019.